2012

Virtual Compton scattering and the generalized polarizabilities of the proton at Q(2)=0.92 and 1.76 GeV2

H. Fonvieille

G. Laveissiere

S. Jaminion

K. Arundell
William & Mary

J. M. Finn
William & Mary

See next page for additional authors

Recommended Citation

Fonvieille, H., Laveissiere, G., Degrande, N., Jaminion, S., Jutier, C., Todor, L., ... & Aniol, K. A. (2012). Virtual Compton scattering and the generalized polarizabilities of the proton at Q 2= 0.92 and 1.76 GeV 2. Physical Review C, 86(1), 015210.

Virtual Compton scattering and the generalized polarizabilities of the proton at $Q^2 = 0.92$ and 1.76 GeV^2

H. Fonvieille,[1,*] G. Laveissière,[1] N. Degrande,[2] S. Jaminion,[1] C. Jutier,[1,3] L. Todor,[3] R. Di Salvo,[1] L. Van Hoorebeke,[2] L. C. Alexa,[4] B. D. Anderson,[5] K. A. Aniol,[6] K. Arundell,[7] G. Audit,[8] L. Auerbach,[9] F. T. Baker,[10] M. Baylac,[8] J. Berthot,[1,†] P. Y. Bertin,[1] W. Bertozzi,[11] L. Bimbot,[12] W. U. Boeglin,[13] E. J. Brash,[4] V. Breton,[1] H. Breuer,[14] E. Burtin,[8] J. R. Calarco,[15] L. S. Cardman,[16] C. Cavata,[8] C.-C. Chang,[14] J.-P. Chen,[16] E. Chudakov,[16] E. Cisbani,[17] D. S. Dale,[18] C. W. de Jager,[16] R. De Leo,[19] A. Deur,[1,16] N. d'Hose,[8] G. E. Dodge,[3] J. J. Domingo,[16] L. Elouadrhiri,[16] M. B. Epstein,[6] L. A. Ewell,[14] J. M. Finn,[7,†] K. G. Fissum,[11] G. Fournier,[8] B. Frois,[8] S. Frullani,[17] C. Furget,[20] H. Gao,[11] J. Gao,[11] F. Garibaldi,[17] A. Gasparian,[18,21] S. Gilad,[11] R. Gilman,[16,22] A. Glamazdin,[23] C. Glashausser,[22] J. Gomez,[16] V. Gorbenko,[23] P. Grenier,[1] P. A. M. Guichon,[8] J. O. Hansen,[16] R. Holmes,[24] M. Holtrop,[15] C. Howell,[25] G. M. Huber,[4] C. E. Hyde,[1,3] S. Incerti,[9] M. Iodice,[17] J. Jardillier,[8] M. K. Jones,[7] W. Kahl,[24] S. Kato,[26] A. T. Katramatou,[5] J. J. Kelly,[14,†] S. Kerhoas,[8] A. Ketikyan,[27] M. Khayat,[5] K. Kino,[28] S. Kox,[20] L. H. Kramer,[13] K. S. Kumar,[29] G. Kumbartzki,[22] M. Kuss,[16] A. Leone,[30] J. J. LeRose,[16] M. Liang,[16] R. A. Lindgren,[31] N. Liyanage,[11] G. J. Lolos,[4] R. W. Lourie,[32] R. Madey,[5] K. Maeda,[28] S. Malov,[22] D. M. Manley,[5] C. Marchand,[8] D. Marchand,[8] D. J. Margaziotis,[6] P. Markowitz,[13] J. Marroncle,[8] J. Martino,[8] K. McCormick,[3] J. McIntyre,[22] S. Mehrabyan,[27] F. Merchez,[20] Z. E. Meziani,[9] R. Michaels,[16] G. W. Miller,[29] J. Y. Mougey,[20] S. K. Nanda,[16] D. Neyret,[8] E. A. J. M. Offermann,[16] Z. Papandreou,[4] B. Pasquini,[33] C. F. Perdrisat,[7] R. Perrino,[30] G. G. Petratos,[5] S. Platchkov,[8] R. Pomatsalyuk,[23] D. L. Prout,[5] V. A. Punjabi,[34] T. Pussieux,[8] G. Quémenér,[1,7] R. D. Ransome,[22] O. Ravel,[1] J. S. Real,[20] F. Renard,[8] Y. Roblin,[1] D. Rowntree,[11] G. Rutledge,[7] P. M. Rutt,[22] A. Saha,[16,†] T. Saito,[28] A. J. Sarty,[35] A. Serdarevic,[4,16] T. Smith,[15] G. Smirnov,[1] K. Soldi,[36] P. Sorokin,[23] P. A. Souder,[24] R. Suleiman,[11] J. A. Templon,[10] T. Terasawa,[28] R. Tieulent,[20] E. Tomasi-Gustaffson,[8] H. Tsubota,[28] H. Ueno,[26] P. E. Ulmer,[3] G. M. Urciuoli,[17] M. Vanderhaeghen,[37] R. L. J. Van der Meer,[4,16] R. Van De Vyver,[2] P. Vernin,[8] B. Vlahovic,[16,36] H. Voskanyan,[27] E. Voutier,[20] J. W. Watson,[5] L. B. Weinstein,[3] K. Wijesooriya,[7] R. Wilson,[38] B. B. Wojtsekhowski,[16] D. G. Zainea,[4] W-M. Zhang,[5] J. Zhao,[11] and Z.-L. Zhou[11]

(The Jefferson Lab Hall A Collaboration)

[1]*Clermont-Université, UBP, CNRS-IN2P3, LPC, BP 10448, F-63000 Clermont-Ferrand, France*

[2]*Department of Physics and Astronomy, Ghent University, B-9000 Ghent, Belgium*

[3]*Old Dominion University, Norfolk, Virginia 23529, USA*

[4]*University of Regina, Regina, SK S4S OA2 Canada*

[5]*Kent State University, Kent Ohio 44242, USA*

[6]*California State University, Los Angeles, Los Angeles, California 90032, USA*

[7]*College of William and Mary, Williamsburg, Virginia 23187, USA*

[8]*CEA IRFU/SPhN Saclay, F-91191 Gif-sur-Yvette, France*

[9]*Temple University, Philadelphia, Pennsylvania 19122, USA*

[10]*University of Georgia, Athens, Georgia 30602, USA*

[11]*Massachusetts Institute of Technology, Cambridge, Massachusetts 02139, USA*

[12]*Institut de Physique Nucléaire (UMR 8608), CNRS/IN2P3-Université Paris-Sud, F-91406 Orsay Cedex, France*

[13]*Florida International University, Miami, Florida 33199, USA*

[14]*University of Maryland, College Park, Maryland 20742, USA*

[15]*University of New Hampshire, Durham, New Hampshire 03824, USA*

[16]*Thomas Jefferson National Accelerator Facility, Newport News, Virginia 23606, USA*

[17]*INFN, Sezione Sanità and Istituto Superiore di Sanità, 00161 Rome, Italy*

[18]*University of Kentucky, Lexington, Kentucky 40506, USA*

[19]*INFN, Sezione di Bari and University of Bari, 70126 Bari, Italy*

[20]*LPSC Grenoble, Universite Joseph Fourier, CNRS/IN2P3, INP, F-38026 Grenoble, France*

[21]*Hampton University, Hampton, Virginia 23668, USA*

[22]*Rutgers, The State University of New Jersey, Piscataway, New Jersey 08855, USA*

[23]*Kharkov Institute of Physics and Technology, Kharkov 61108, Ukraine*

[24]*Syracuse University, Syracuse, New York 13244, USA*

[25]*Duke University, Durham, North Carolina 27706, USA*

[26]*Yamagata University, Yamagata 990, Japan*

[27]*Yerevan Physics Institute, Yerevan 375036, Armenia*

[28]*Tohoku University, Sendai 980, Japan*

[29]*Princeton University, Princeton, New Jersey 08544, USA*

[30]*INFN, Sezione di Lecce, 73100 Lecce, Italy*

[31]*University of Virginia, Charlottesville, Virginia 22901, USA*

[32]*State University of New York at Stony Brook, Stony Brook, New York 11794, USA*

[33]*Dipartimento di Fisica, Università degli Studi di Pavia, and INFN, Sezione di Pavia, Italy*

[34]*Norfolk State University, Norfolk, Virginia 23504, USA*
[35]*Florida State University, Tallahassee, Florida 32306, USA*
[36]*North Carolina Central University, Durham, North Carolina 27707, USA*
[37]*Institut fuer Kernphysik, Johannes Gutenberg University, D-55099 Mainz, Germany*
[38]*Harvard University, Cambridge, Massachusetts 02138, USA*
(Received 18 May 2012; published 25 July 2012)

Virtual Compton scattering (VCS) on the proton has been studied at the Jefferson Laboratory using the exclusive photon electroproduction reaction $ep \to ep\gamma$. This paper gives a detailed account of the analysis which has led to the determination of the structure functions $P_{LL} - P_{TT}/\epsilon$ and P_{LT} and the electric and magnetic generalized polarizabilities (GPs) $\alpha_E(Q^2)$ and $\beta_M(Q^2)$ at values of the four-momentum transfer squared $Q^2 = 0.92$ and 1.76 GeV^2. These data, together with the results of VCS experiments at lower momenta, help building a coherent picture of the electric and magnetic GPs of the proton over the full measured Q^2 range and point to their nontrivial behavior.

DOI: 10.1103/PhysRevC.86.015210 PACS number(s): 13.60.Fz, 14.20.Dh, 24.85.+p

I. INTRODUCTION

The nucleon is a composite object, and understanding its structure is the subject of intensive efforts. Its electromagnetic structure is cleanly probed by real and virtual photons. Real Compton scattering (RCS) at low energy gives access to the nucleon polarizabilities, which describe how the charge, magnetization, and spin densities in the nucleon are deformed when the particle is subjected to an external quasistatic electromagnetic field.

Virtual Compton scattering (VCS) $\gamma^* N \to \gamma N$ gives access to the generalized polarizabilities (GPs). Being dependent on the photon virtuality Q^2, these observables parametrize the *local* polarizability response of the system, i.e., they give information on the density of polarization inside the nucleon. Experimental information on the GPs is obtained through the reaction of exclusive photon electroproduction. Several dedicated experiments on the proton

$$e\,p \;\to\; e\,p\,\gamma \tag{1}$$

have been performed at various Q^2 and in the low-energy regime. This includes the near-threshold region, where the center-of-mass energy W of the (γp) system is below the one-pion threshold [$W < (m_p + m_{\pi^0})$, where m_p and m_{π^0} are the proton and pion masses] and up to the $\Delta(1232)$ resonance region. Process (1) has been studied experimentally at the Mainz Microton (MAMI) [1–4], the Thomas Jefferson National Accelerator Facility (JLab) [5,6], and MIT-Bates [7,8].

The results of the near-threshold VCS data analysis of the JLab VCS experiment E93-050, i.e., the structure functions $P_{LL} - P_{TT}/\epsilon$ and P_{LT}, and the electric and magnetic GPs α_E and β_M at $Q^2 = 0.92$ and 1.76 GeV^2, have been published elsewhere [5]. However, analysis details and cross-section data were not given. This is the aim of the present paper, which is organized as follows. After recalling briefly the theoretical concepts in Sec. II, the experimental setup is described in Sec. III. Section IV reports about data analysis, including event reconstruction, acceptance calculation, and cross-section determination. Section V presents the measured cross section, the physics results deduced from the various analyses, and a discussion. A short conclusion ends the paper in Sec. VI.

II. THEORETICAL CONCEPTS AND TOOLS FOR EXPERIMENTS

This section summarizes the theoretical concepts underlying the measurements of VCS at low energy: the GPs, the structure functions, and the principles of measurement. For details, we refer to review papers [9–11] (theory) and [12–16] (experiments).

A. Generalized polarizabilities

Polarizabilities are fundamental characteristics of any composite system, from hadrons to atoms and molecules. They describe how the system responds to an external quasistatic electromagnetic field. RCS yields for the static polarizabilities of the proton [17] are as follows:

$$\alpha_E(\text{electric}) = (12.1 \pm 0.3_{\text{stat}} \mp 0.4_{\text{syst}}) \times 10^{-4}\ \text{fm}^3$$
$$\beta_M(\text{magnetic}) = (1.6 \pm 0.4_{\text{stat}} \pm 0.4_{\text{syst}}) \times 10^{-4}\ \text{fm}^3.$$

These values are much smaller than the particle's volume and indicate that the proton is a very stiff object, due to the strong binding between its constituents.

The formalism of VCS on the nucleon was early explored in Ref. [18] and the concept of generalized polarizabilities was first introduced in Ref. [19] for nuclei. The nucleon case was established within a low energy theorem (LET), first applied to VCS by P. Guichon *et al.* in Ref. [20]. This development paved the way to new experimental investigations: It became possible to explore the spatial distribution of the nucleon's polarizability response, which is in essence the physical meaning of the GPs (see, e.g., Refs. [21,22]).

Photon electroproduction accesses VCS via the amplitude decomposition shown in Fig. 1: $T^{ep\gamma} = T^{\text{BH}} + T^{\text{VCSBorn}} + T^{\text{VCSNon-Born}}$, where BH stands for the Bethe-Heitler process. Formally, the GPs are obtained from the multipole decomposition of the Non-Born amplitude $T^{\text{VCSNon-Born}}$ taken in the "static field" limit $q'_{\text{c.m.}} \to 0$, where $q'_{\text{c.m.}}$ is the momentum of

*Corresponding author: helene@clermont.in2p3.fr
†Deceased.

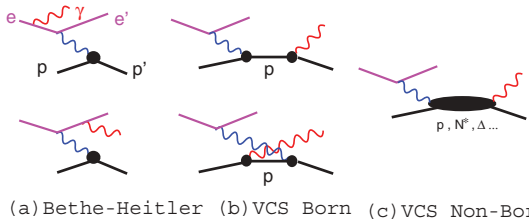

FIG. 1. (Color online) Feynman graphs of photon electroproduction.

the final real photon in the γp center of mass (noted as CM hereafter). The GPs are functions of $q_{\text{c.m.}}$, the momentum of the virtual photon in the CMor, equivalently, the photon virtuality Q^2 (see Appendix A for more details). After the work of Drechsel *et al.* [23,24], six independent GPs remain at lowest order. Their standard choice is given in Table I, where they are indexed by the EM transitions involved in the Compton process. Since this paper mainly focuses on the electric and magnetic GPs, i.e., the two scalar ones (or spin-independent, or non-spin-flip, $S = 0$; see Table I), we recall their definition,

$$\alpha_E(Q^2) = -P^{(L1,L1)0}(Q^2)\left(\frac{e^2}{4\pi}\sqrt{\frac{3}{2}}\right),$$
$$\beta_M(Q^2) = -P^{(M1,M1)0}(Q^2)\left(\frac{e^2}{4\pi}\sqrt{\frac{3}{8}}\right).$$

These GPs coincide in the limit $Q^2 \to 0$ with the usual static RCS polarizabilities α_E and β_M introduced above.

B. Theoretical models and predictions

There are a number of theoretical models which describe and calculate the GPs of the nucleon. They include heavy baryon chiral perturbation theory (HBChPT) [25–27], nonrelativistic quark constituent models [20,28–30], dispersion relations [10,31,32], the linear-σ model [33,34], the effective Lagrangian model [35], the Skyrme model [36], the covariant framework of Ref. [37], or more recent works regarding GPs redefinition [38], manifestly Lorentz-invariant baryon ChPT [39], or light-front interpretation of GPs [22].

One of the main physical interests of GPs is that they can be sensitive in a specific way to the various physical degrees of freedom, e.g., the nucleon core and the meson cloud. Thus, their knowledge can bring novel information about nucleon structure. The electric GP is usually predicted to have a smooth falloff with Q^2. The magnetic GP has two contributions of paramagnetic and diamagnetic origin; they nearly cancel, making the total magnitude small. As will be shown in Sec. V C, the available data more or less confirm these trends. A synthesis of diverse GP predictions for the proton is presented in Ref. [30].

TABLE I. The standard choice for the nucleon GPs. In the notation of the first column, $\rho(\rho')$ refers to the magnetic (1) or longitudinal (0) nature of the initial (final) photon, $L(L')$ represents the angular momentum of the initial (final) photon, and S differentiates between the spin-flip ($S = 1$) and non-spin-flip ($S = 0$) character of the transition at the nucleon side. The multipole notation in the second column uses the magnetic (M) and longitudinal (L) multipoles. The six listed GPs correspond to the lowest possible order in $q'_{\text{c.m.}}$, i.e., a dipole final transition ($L' = 1$). The third column gives the correspondence in the RCS limit ($Q^2 \to 0$ or $q_{\text{c.m.}} \to 0$).

$P^{(\rho' L', \rho L)S}(q_{\text{c.m.}})$	$P^{(f,i)S}(q_{\text{c.m.}})$	RCS limit
$P^{(01,01)0}$	$P^{(L1,L1)0}$	$-\frac{4\pi}{e^2}\sqrt{\frac{2}{3}}\,\alpha_E$
$P^{(11,11)0}$	$P^{(M1,M1)0}$	$-\frac{4\pi}{e^2}\sqrt{\frac{8}{3}}\,\beta_M$
$P^{(01,01)1}$	$P^{(L1,L1)1}$	0
$P^{(11,11)1}$	$P^{(M1,M1)1}$	0
$P^{(01,12)1}$	$P^{(L1,M2)1}$	$-\frac{4\pi}{e^2}\frac{\sqrt{2}}{3}\,\gamma_3$
$P^{(11,02)1}$	$P^{(M1,L2)1}$	$-\frac{4\pi}{e^2}\frac{2\sqrt{2}}{3\sqrt{3}}(\gamma_2+\gamma_4)$

C. The low-energy theorem and the structure functions

The LET established in Ref. [20] is a major tool for analyzing VCS experiments. The LET describes the photon electroproduction cross section below the pion threshold in terms of GPs. The (unpolarized) $ep \to ep\gamma$ cross section at small $q'_{\text{c.m.}}$ is written as

$$d^5\sigma = d^5\sigma^{\text{BH+Born}} + q'_{\text{c.m.}}\phi\Psi_0 + O\left(q'^2_{\text{c.m.}}\right). \tag{2}$$

The notation $d^5\sigma$ stands for $d^5\sigma/dk'_{\text{elab}}d\Omega'_{\text{elab}}d\Omega_{\text{c.m.}}$, where k'_{elab} is the scattered electron momentum, $d\Omega'_{\text{elab}}$ its solid angle, and $d\Omega_{\gamma\text{c.m.}}$ the solid angle of the outgoing photon (or proton) in the CM; ϕ is a phase-space factor. The (BH + Born) cross section is known and calculable, with the proton electromagnetic form factors G_E^p and G_M^p as inputs. The Ψ_0 term represents the leading polarizability effect. It is given by

$$\Psi_0 = v_1\left(P_{LL} - \frac{1}{\epsilon}P_{TT}\right) + v_2 P_{LT}, \tag{3}$$

where P_{LL}, P_{TT}, and P_{LT} are three unknown structure functions containing the GPs, ϵ is the usual virtual photon polarization parameter, and v_1, v_2 are kinematical coefficients depending on $(q_{\text{c.m.}}, \epsilon, \theta_{\text{c.m.}}, \varphi)$ (see Ref. [9] for their full definition). The incoming photon is chosen to point in the z direction. The Compton angles are the polar angle $\theta_{\text{c.m.}}$ of the outgoing photon in the CM and the azimuthal angle φ between the leptonic and hadronic planes; see Fig. 2.

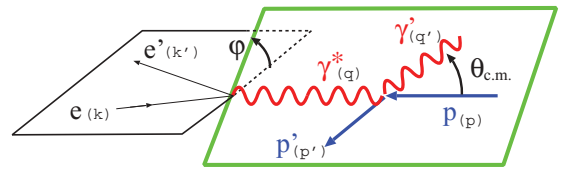

FIG. 2. (Color online) $(ep \to ep\gamma)$ kinematics; four-momentum vectors notation and Compton angles $(\theta_{\text{c.m.}}, \varphi)$ in the γp center of mass.

The expressions of the structure functions useful to the present analysis are summarized here,

$$P_{LL} = \frac{4m_p}{\alpha_{\rm em}} G_E^p(Q^2)\alpha_E(Q^2), \quad P_{TT} = [P_{\rm TTspin}],$$
$$P_{LT} = -\frac{2m_p}{\alpha_{\rm em}}\sqrt{\frac{q^2_{\rm c.m.}}{Q^2}} G_E^p(Q^2)\beta_M(Q^2) + [P_{\rm LTspin}], \tag{4}$$

where $\alpha_{\rm em}$ is the fine structure constant. The terms in square brackets are the spin part of the structure functions (i.e., containing only spin GPs) and the other terms are the scalar parts. The important point is that the electric and magnetic GPs enter only in P_{LL} and in the scalar part of P_{LT}, respectively.

In an unpolarized experiment at fixed Q^2 and fixed ϵ, such as ours, only two observables can be determined using the LET: $P_{LL} - P_{TT}/\epsilon$ and P_{LT}, i.e., only two specific combinations of GPs. To further disentangle the GPs, one can, in principle, make an ϵ separation of P_{LL} and P_{TT} (although difficult to achieve), and, in order to extract all individual GPs, one has to resort to double polarization [40]. Here we perform a LET or LEX (for low-energy expansion) analysis in the following way: The two structure functions $P_{LL} - P_{TT}/\epsilon$ and P_{LT} are extracted by a linear fit of the difference $d^5\sigma^{\rm exp} - d^5\sigma^{\rm BH+Born}$, based on Eqs. (2) and (3), and assuming the validity of the truncation of the expansion to $O(q'^2_{\rm c.m.})$. Then, to further isolate the scalar part in these structure functions, i.e., to access $\alpha_E(Q^2)$ and $\beta_M(Q^2)$, a model input is required, since the spin part is not known experimentally.

D. The dispersion relations model

The dispersion relation (DR) approach is the second tool for analyzing VCS experiments. It is of particular importance in our case, so we briefly review its properties in this section. The DR formalism was developed by B. Pasquini *et al.* [10,32] for RCS and VCS. Contrary to the LET, which is limited to the energy region below the pion threshold, the DR formalism is also valid in the energy region up to the $\Delta(1232)$ resonance—an advantage fully exploited in our experiment.

The Compton tensor is parametrized through 12 invariant amplitudes $F_i (i = 1, \ldots, 12)$. The GPs are expressed in terms of the Non-Born part $F_i^{\rm Non\text{-}Born}$ of these amplitudes at the point $t = -Q^2, \nu = (s-u)/4m_p = 0$, where s, t, u are the Mandelstam variables of the Compton scattering. The $F_i^{\rm Non\text{-}Born}$ amplitudes, except for two of them, fulfill unsubtracted dispersion relations. When working in the energy region up to the $\Delta(1232)$, these s-channel integrals are considered to be saturated by the πN intermediate states. In practice, the calculation uses the MAID pion photo- and electroproduction multipoles [41], which include both resonant and nonresonant production mechanisms.

The amplitudes F_1 and F_5 have an unconstrained part, corresponding to asymptotic contributions and dispersive contributions beyond πN. For F_5 this part is dominated by the t-channel π^0 exchange; with this input, all four spin GPs are fixed in the model. For F_1, a main feature is that in the limit $(t = -Q^2, \nu = 0)$ its Non-Born part is proportional to the magnetic GP. The unconstrained part of $F_1^{\rm Non\text{-}Born}$ is estimated by an energy-independent function noted $\Delta\beta$ and phenomenologically associated with the t-channel σ-meson exchange. This leads to the expression

$$\beta_M(Q^2) = \beta^{\pi N}(Q^2) + \Delta\beta(Q^2), \tag{5}$$

where $\beta^{\pi N}$ is the dispersive contribution calculated using MAID multipoles. The $\Delta\beta$ term is parametrized by a dipole form

$$\Delta\beta = \frac{[\beta^{\rm exp} - \beta^{\pi N}]_{Q^2=0}}{\left(1 + Q^2/\Lambda_\beta^2\right)^2}. \tag{6}$$

An unconstrained part is considered also for a third amplitude, F_2. Since in the limit $(t = -Q^2, \nu = 0)$ the Non-Born part of F_2 is proportional to the sum $(\alpha_E + \beta_M)$, one finally ends with a decomposition similar to Eq. (6) for the electric GP itself,

$$\alpha_E(Q^2) = \alpha^{\pi N}(Q^2) + \Delta\alpha(Q^2),$$
$$\text{with} \quad \Delta\alpha = \frac{[\alpha^{\rm exp} - \alpha^{\pi N}]_{Q^2=0}}{\left(1 + Q^2/\Lambda_\alpha^2\right)^2}. \tag{7}$$

The implication for experiments is that in the DR model the two scalar GPs are not fixed. They depend on the free parameters Λ_α and Λ_β (dipole masses), which can be fitted from the data. It must be noted that the choice of a dipole form in Eqs. (6) and (7) is arbitrary: Λ_α and Λ_β only play the role of intermediate quantities in order to extract VCS observables, with minimal model dependence. These parameters are not imposed to be constant with Q^2. Our experimental DR analysis consists in adjusting Λ_α and Λ_β by a fit to the measured cross section, separately in our two Q^2 ranges. Then, in each Q^2 range, the model is entirely constrained; it provides all VCS observables at a given value of Q^2 representative of the range: the scalar GPs as well as the structure functions, in particular $P_{LL} - P_{TT}/\epsilon$ and P_{LT}.

III. THE EXPERIMENT

The photon electroproduction cross section is small and requires high-performance equipment to be measured with accuracy. To ensure the exclusivity of the reaction, one must detect at least two of the three particles in the final state. The chosen technique is to perform electron scattering at high luminosity on a dense proton target and detect, in coincidence, the two outgoing charged particles in magnetic spectrometers of high resolution and small solid angle. These devices ensure a clean detection and a good identification of process (1). Section III describes how the experiment was designed and realized using the CEBAF electron beam and the JLab Hall A equipment.

A. Apparatus

Since the Hall was in its commissioning phase at the time of the data taking for this experiment (1998), not all devices were fully operational and the minimal number of detectors were used. However, the experiment fully exploited

the main capabilities of the accelerator and the basic Hall equipment: 100% duty cycle, high-resolution spectrometers, and high luminosities. The Hall A instrumentation is described extensively in Ref. [42] and in several thesis works related to the experiment [43–47]. Only a short overview is given here, and some specific details are given in the subsections.

The continuous electron beam at 4 GeV energy (unpolarized) was sent to a 15-cm-long liquid hydrogen target. The two High Resolution Spectrometers, noted here as HRS-E and HRS-H, were used to detect in coincidence an outgoing electron and proton, respectively. After exiting the target region, the particles in each HRS encounter successively the entrance collimator of 6 msr, the magnetic system (QQDQ), and the detector package. The latter consisted of a set of four vertical drift chambers (VDC) followed by two scintillator planes S1 and S2. It was complemented in the HRS-E by a Cerenkov detector and a shower counter and in the HRS-H by a focal plane polarimeter. The VDCs provided particle tracking in the focal plane. The scintillators were the main trigger elements. They provided the timing information in each spectrometer and allowed formation of the coincidence trigger.

B. Kinematical settings and data taking

Data were taken in two different Q^2 ranges, near 0.9 and 1.8 GeV^2. The corresponding data sets are labeled I and II, respectively. At $Q^2 = 0.9$ GeV^2 dedicated data were taken in the region of the nucleon resonances [6]. This leads us to split data set I into two independent subsets, I-a and I-b, according to the W range. Figure 3 displays the various domains covered in W or, equivalently, $q'_{\text{c.m.}}$. Data sets I-a and II have events essentially below the pion threshold, while data set I-b is more focused on the $\Delta(1232)$ resonance region and above. For the analyses presented here, emphasis will be put on data sets I-a and II. For data set I-b, details can be found in Ref. [6], in which a nucleon resonance study was performed to $W = 2$ GeV. Here, the lowest-W part of data set I-b is analyzed in terms of GPs. Table II summarizes our notations.

For each of the data sets I-a and II, the HRS-E setting was kept fixed, while the HRS-H setting was varied in momentum and angle. In process (1) the final proton is emitted in the laboratory system inside a cone of a few degrees around the direction of the virtual photon, thanks to a strong CM-to-Lab Lorentz boost. Therefore, with a limited number of settings (and in-plane spectrometers), one can cover most of the desired phase space, including the most out-of-plane angles. As an example, Fig. 4 illustrates the configuration of the HRS-H settings for data set I-a. In addition, in the HRS-E the momentum setting is chosen in order to have the VCS events in the center of the acceptance, i.e., near $\delta p/p = 0\%$. As a result, the elastic peak from $ep \to ep$ scattering may also be in the acceptance of this spectrometer (at higher $\delta p/p$), especially when W is low, i.e., for data sets I-a and II. In this case, electrons elastically scattered from hydrogen are seen in the HRS-E single-arm events, although they are kinematically excluded from the true coincidences.

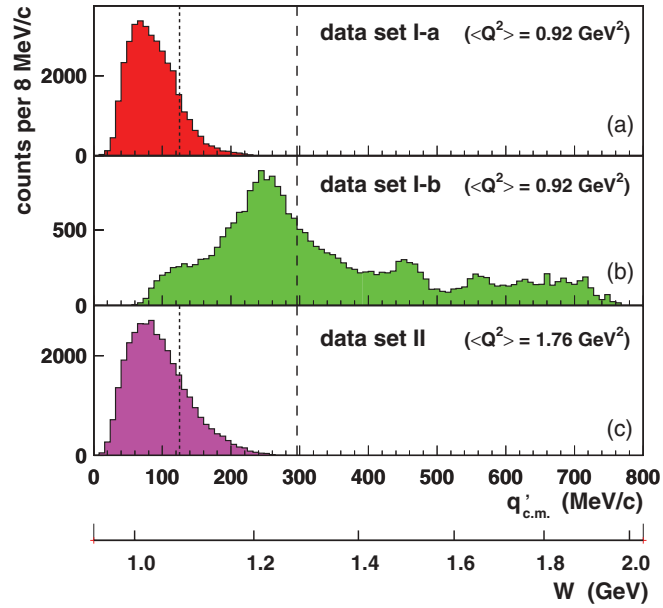

FIG. 3. (Color online) The range in $q'_{\text{c.m.}}$, or W, covered by the various data sets for the $ep \to ep\gamma$ events. The vertical lines show the upper limit applied in the analyses: the pion threshold (dotted line at $W = 1.073$ GeV) for the LEX analyses and $W = 1.28$ GeV (dashed line) for the DR analyses. W and $q'_{\text{c.m.}}$ are related by $W = q'_{\text{c.m.}} + \sqrt{q'^2_{\text{c.m.}} + m_p^2}$.

Data acquisition was performed with the CODA software developed by the Continuous Electron Beam Accelerator Facility (CEBAF) [48]. The trigger setup includes several types, among which T1 and T3 are single-arm HRS-E and HRS-H good triggers. The T5 triggers, formed by the coincidence between T1 and T3, are the main ones used in the physics analysis. For each event the raw information from the detectors and the beam position devices is written on file. Scalers containing trigger rates and integrated beam charge are inserted periodically into the data stream, as well as various parameters from the EPICS slow control system. Special runs were recorded to study spectrometer optics.

IV. DATA ANALYSIS

This section describes the main steps that were necessary to reach the accurate measurement of the $(ep \to ep\gamma)$ differential

TABLE II. The various data sets of the experiment. Columns 2 and 3 give the ranges in Q^2 and W covered by the experiment. The fixed value of Q^2 chosen in the analyses is 0.92 GeV^2 (respectively, 1.76 GeV^2) for data sets I-a and I-b (respectively, II). Columns 4 and 5 give the W range used in the LEX and DR analyses.

Data set	Q^2 range (GeV^2)	W range (GeV)	W range LEX (GeV)	W range DR (GeV)
I-a	[0.85, 1.15]	[0.94, 1.25]	[0.94, 1.07]	[0.94, 1.25]
I-b	[0.85, 1.15]	[1.00, 2.00]	–	[1.00, 1.28]
II	[1.60, 2.10]	[0.94, 1.25]	[0.94, 1.07]	[0.94, 1.25]

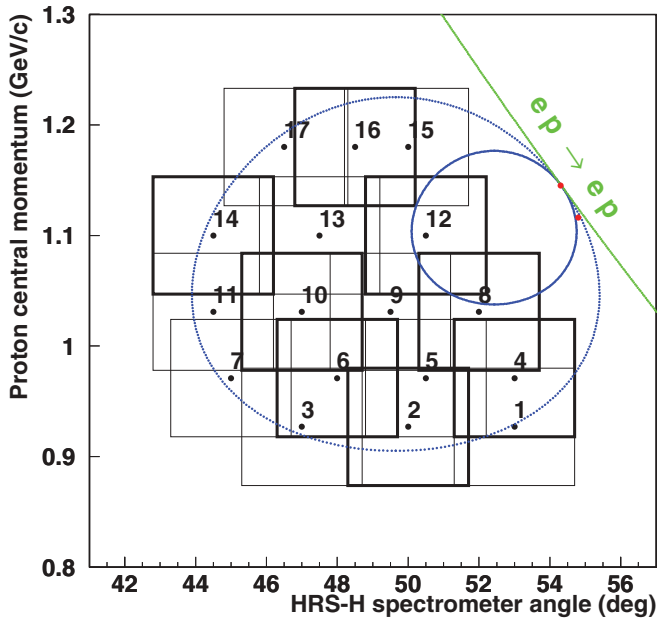

FIG. 4. (Color online) The 17 HRS-H settings for the proton detection in data set I-a. Each setting is represented by a box in momentum and angle. The closed curves correspond to in-plane $ep \rightarrow ep\gamma$ kinematics at fixed values of $q'_{\text{c.m.}}$: 45 MeV/c (inner curve) and 105 MeV/c (outer curve). The $ep \rightarrow ep$ elastic line is also drawn at a beam energy of 4.045 GeV.

cross section: raw-level processing, event reconstruction, analysis cuts, and acceptance calculation.

A. Beam charge, target density, and luminosity

The electron beam current is measured by two resonant cavities (Beam Charge Monitors, BCM) placed upstream of the Hall A target. The signal of each cavity is sent to different electronic chains. In the experiment, the main measurement of the beam charge used the upstream cavity and the chain consisting of a rms-to-dc converter followed by a voltage-to-frequency converter (VtoF), generating pulses that are counted by a scaler. The content of the VtoF scaler was written on the runfile every 10 s. At the end of each run one obtained in this way the integrated charge of the run. The BCM were calibrated twice a day against the Unser monitor, located between the two cavities and measuring the beam current in absolute. The procedure also implied the offline calibration of the VtoF converter. Beam currents ranged from 30 to 100 μA with an average of 70 μA, and the integrated charge per run was determined with an accuracy of 0.5%.

The experiment used the 15-cm-long liquid hydrogen cell ("beer can"). It was kept at a constant temperature $T = 19.0$ K and pressure $P = 1.725$ bar, yielding a density $\rho_0 = 0.0723$ g cm^{-3} at zero beam current [49]. The beam was rastered on the target in both transverse directions in order to avoid local boiling of the hydrogen. Studies based on the data of this experiment [45] showed that density losses reached at maximum 1% for a beam current of 100 μA, so the target boiling effect was considered to be negligible and the density was taken equal to ρ_0 in the analyses.

The luminosity $\mathcal{L}$ needed for cross-section measurements is obtained on a run-per-run basis. Based on the above considerations, it is determined with an accuracy of $\sim\pm 1\%$. Typical values of instantaneous luminosities are of the order of 2 to 4 $\times$ 10^{38} cm^{-2} s^{-1}.

B. Rate corrections

The raw event rate is obtained by counting the number of T5 events, i.e., the coincidence triggers between the two spectrometers. Several correction factors have to be applied to this rate.

The first correction is due to trigger inefficiency, coming from the scintillators of the detector package. It is obtained by studying the single-arm "junk triggers" T2 (electron side) and T4 (hadron side), which record all configurations other than normal in the scintillators. The normal configuration (T3 or T5) is a coincidence between paddles in the S1 and S2 planes in an allowed geometrical configuration ("S-ray"), each paddle signal requiring the coincidence between its left and right phototubes. Among the junk triggers, there are some good events, typically with a hit missing in the scintillator paddles. We identify them by use of a "clean-up" procedure, consisting in the additional requirement of a valid track in the VDCs and a Cerenkov signal in the electron arm. The scintillator inefficiency is then defined as the number of such good T2 or T4 events, relative to the number of (T1 + T5) or (T3 + T5) events in the same clean-up conditions. The inefficiency is calculated independently for both planes S1 and S2 in each arm. It is binned in the x (dispersive) and y (transverse) coordinates in each plane to account for local variations. The observed inefficiency was usually of the order of 1%, reaching occasionally 10% locally in the electron arm [50]. This commissioning problem was fixed after our experiment.

The second correction concerns the acquisition dead time. For each run, a scaler counts the number S_5 of T5 events at the output of the trigger logic. Among these events, only N_5 ($<S_5$) are written on file due to the dead time of the [acquisition + computer] system. The correction consists in multiplying the event rate by the ratio S_5/N_5. The dead time depends on the beam current; it varied between 5 and 40% in the experiment.

The third correction comes from the dead time of the trigger electronics itself (EDT). It was not measured directly during the experiment but determined afterward. The EDT estimation is based on a fit to the actual rates in the scintillator paddles, using the strobe rate of each spectrometer. This fit was established in later experiments when the strobe rate was inserted into the data stream [51]. The resulting correction is of the order of 1–3% in our case. The tracking inefficiency is considered to be negligible, in the sense that, for a real particle, the tracking algorithm basically always finds at least one track in the focal plane, which allows us to process the event further. This is due to the good efficiency per wire in the VDCs. Finally, another small correction of the order of 1% is applied to

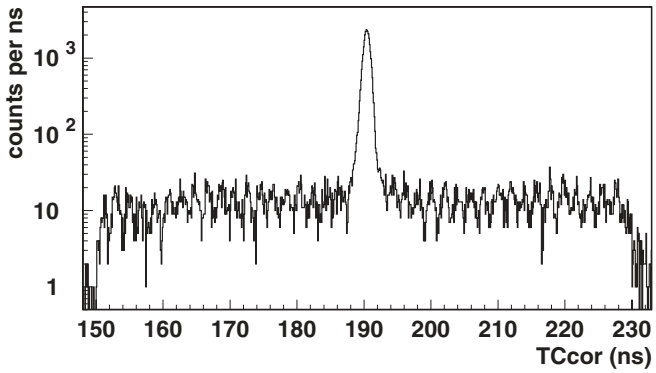

FIG. 5. Coincidence time spectrum of data set I-a. The central peak is 0.5 ns wide in rms.

account for the losses of protons by nuclear interactions in the target and spectrometer windows. The uncertainty on the event rate, after having corrected for all the above inefficiencies, is estimated to be smaller than 0.5% in relative.

C. Event reconstruction

The Hall A analyzer ESPACE processes the raw detector signals and builds all the first-level variables of the event: coincidence time, beam position on target, three-momentum vector of the detected particles at the vertex point, and so on. Figure 5 shows a typical coincidence time spectrum between the HRS-E and HRS-H. The central peak allows us to select the true coincidences. Random coincidences under the peak are subtracted using side bands. In the plateau one clearly sees the 2-ns microstructure of the beam, corresponding to Hall A receiving one-third of the pulses of the 1497-GHz cw beam.

In the analyses presented here, particle identification in the detectors is basically not needed. This is because the kinematical settings of VCS near threshold (cf. Table III) are close to ep elastic scattering; therefore, the true coincidences between the two spectrometers are essentially (e, p) ones. The other true coincidences that could be considered are of the type (e^-, π^+) or (π^-, p), coming from single or multiple pion production processes. However, such events either do not match the acceptance settings (case of single charged-pion electroproduction) or yield missing masses which are beyond one pion mass, i.e., far from the VCS region of interest (case of multiple pion production). Therefore, detectors such as the gas Cerenkov counter or the electromagnetic calorimeter in the HRS-E were essentially not used, and only the information from the VDCs and the scintillators in both arms were treated. As a verification, however, the analysis of data set II was performed with and without requiring a signal in the Cerenkov counter in the HRS-E, and the results were found unchanged.

TABLE III. Summary of the kinematical settings for each data set. The nominal beam energy is $E_{\text{beam}} = 4.045$ GeV (see Sec. IV D for actual values). p_e and θ_e are the central momentum of the HRS-E spectrometer and its angle with respect to the beamline (electron side). p_p and θ_p are the same variables on the proton side, i.e., for the HRS-H spectrometer.

Data set	p_e (GeV/c)	θ_e (°)	p_p (GeV/c)	θ_p (°)
I-a	3.43	15.4	[0.93, 1.19]	[45, 53]
I-b	[3.03, 3.26]	[15.7, 16.4]	[1.31, 1.53]	[37, 45]
II	2.93	23.0	[1.42, 1.76]	[37, 42]

Due to the extended size of the target and the rather large raster size ($\sim\pm$3–5 mm in both directions), it is important to know the interaction point inside the hydrogen volume for each event. This point is characterized by its coordinates (x_v, y_v, z_v) in the Hall A laboratory frame. The coordinates transverse to the beam axis, horizontal x_v and vertical y_v, are obtained from the two BPMs located upstream the target. It turned out that for a large fraction of the data taking, the BPM information was accidentally desynchronized from the event recorded by CODA. A special resynchronization procedure [46,52] was established offline by coupling the BPM to the raster information (which is always synchronized with the event). The BPMs then could be used, yielding x_v and y_v in absolute to better than $\pm$0.5 mm event per event.

The calculation of the longitudinal coordinate z_v requires information from the spectrometers. It is obtained by intersecting the beam direction with the track of one of the two detected particles. For this task the HRS-E was chosen, since it has the best resolution in horizontal coordinate, i.e., the variable noted y_{tg} in the spectrometer frame. The resolution in y_{tg} is excellent, about 0.6 mm in rms for the HRS-E (and twice larger for the HRS-H).

The particle reconstruction proceeds as follows. In each arm the particle's trajectory is given by the VDCs in the focal plane. This "golden track" is characterized by four independent variables $(x, y, \theta, \varphi)_{\text{fp}}$. These variables are combined with the optic tensor of the spectrometer to yield four independent variables at the target: the relative momentum $\delta p/p$, the horizontal coordinate y_{tg}, and the projected horizontal and vertical angles, θ_{tg} and φ_{tg}, in the spectrometer frame. A fifth variable, x_{tg}, characterizing the vertical extension of the track, is calculated using the beam vertical position and allows us to compute small extended-target corrections to the dispersive variables θ_{tg} and $\delta p/p$. The total energy of the particle is then determined from its momentum and its assumed nature (e in HRS-E or p in HRS-H). It is further corrected for energy losses in all materials, from the interaction point to the spectrometer entrance. At this level, the four-momentum vectors of the incoming electron, scattered electron, and outgoing proton, k, k', and p', respectively, are known at the vertex point. One can then compute the full kinematics of the reaction $ep \to epX$ and a number of second-level variables.

For the physics analyses, the main reconstructed variables are Q^2, W, ϵ, and $q_{\text{c.m.}}$ on the lepton side and the four-momentum vector of the missing system X: $p_X = k + p - k' - p'$. This four-vector is transformed from the laboratory frame to the CM, where one calculates the angles of the missing momentum vector $\vec{p}_{X\text{c.m.}}$ with respect to the virtual photon momentum vector $\vec{q}_{\text{c.m.}}$. These angles, polar $\theta_{\text{c.m.}}$ and

azimuthal φ (see Fig. 2), and the modulus of the missing momentum, which represents $q'_{\text{c.m.}}$ in the case of VCS, are the three variables used to bin the cross section.

Other second-level variables are important for the event selection as well as for the experimental calibration. The first one is the missing mass squared $M_X^2 = (k + p - k' - p')^2$. In the experimental M_X^2 spectrum, a photon peak and a π^0 peak are observed, corresponding to the physical processes $ep \to ep\gamma$ and $ep \to ep\pi^0$ (see Fig. 7). A cut in M_X^2 is, thus, necessary to select the reaction channel.

Two other variables, of geometrical nature, have proven to be useful. The first one, x_{dif}, compares two independent determinations of the horizontal coordinate of the vertex point in the Hall A laboratory frame: the one measured by the BPMs (x_v) and the one obtained by intersecting the two tracks measured by the spectrometers and called $x_{2\text{arms}}$. The distribution of the difference $x_{\text{dif}} = x_{2\text{arms}} - x_v$ is expected to be a narrow peak centered on zero. The second geometrical variable, Y_{dif}, will be described in Sec. IV E.

D. Experimental calibration

A lot of experimental parameters have to be well calibrated. At the time of the experiment, the existing optic tensors of the spectrometers were not fully adapted to an extended target; it was necessary to optimize them. Using dedicated runs, new optic tensors were determined for the VCS analysis [53]. They were obtained in both arms for our designed momentum range, and they clearly improved the resolution of the event reconstruction.

A number of offsets, of either geometrical or kinematical origin, also had to be adjusted. Among the geometrical offsets, some were given by the CEBAF surveys, such as the target and collimator positions. Others, such as the mispointing of the spectrometers, were recorded in the data stream, but their reading was not always reliable and some of them had to be adjusted by software. One should note that not all offsets have to be known in absolute; what is needed is the relative coherence among target position, beam position, and spectrometer mispointing. The consistency checks were made on the distribution of the z_v and x_{dif} variables (defined in Sec. IV C) for real events. The main geometrical offset was found to be a horizontal mispointing of the HRS-E by 4 mm.

The kinematical offsets consist in small systematic shifts in the reconstructed momentum and angles of the particles at the vertex point. They are mainly due to (i) a beam energy uncertainty (the beam energy measurements described in Ref. [42] were not yet operational), (ii) residual biases in the optic tensors, and (iii) field reproducibility in the spectrometer magnets. The adjustment of these offsets is based on the optimization of the peaks in missing mass squared, in width and position, for the two reactions $ep \to ep\gamma$ and $ep \to ep\pi^0$ simultaneously. This procedure yields a coherent set of offsets for each setting [54]. An overview of the results is presented in Table IV. All kinematical offsets were found to be small, except for the beam energy, which was significantly below the nominal value from the accelerator by about 10–16 MeV (see Fig. 6).

TABLE IV. Global results for the fitted offsets on the seven variables: beam energy, particle momenta (p_e, p_p) and particle angles. $\varphi_{\text{tg}(e)}$, $\varphi_{\text{tg}(p)}$ [respectively, $\theta_{\text{tg}(e)}$, $\theta_{\text{tg}(p)}$] are the horizontal (respectively, vertical) angles of the particle's track in the spectrometer frame. Some offsets have to be fixed in order to ensure the fit stability [54]. The range in brackets indicates setting-to-setting variations of the offsets.

Variable	Range found for the offset	Estimated uncertainty on the offset
E_{beam}	$[-16, -10]$ MeV	± 2 MeV
p_e	0 (fixed)	± 0.3 MeV/c
p_p	$[-1.5, +1.5]$ MeV/c	± 0.5 MeV/c
$\varphi_{\text{tg}(e)}$	$[0, +0.1]$ mr	± 0.3 mr
$\varphi_{\text{tg}(p)}$	$[-1.7, -0.7]$ mr	± 0.3 mr
$\theta_{\text{tg}(e)}$	$[-1.6, -0.5]$ mr	± 0.5 mr
$\theta_{\text{tg}(p)}$	0 (fixed)	± 0.5 mr

E. Analysis cuts

The offsets described above were established using clean event samples. However, the raw coincidences are not so clean, as can be seen, e.g., from the spectrum in the inset of Fig. 7 (top). The photon peak is contaminated by a large broad bump centered near $-15\,000$ MeV^2. These events are mostly due to ep elastic scattering with the final proton "punching through" the HRS-H entrance collimator. They require specific cuts in order to be eliminated. A key condition for the VCS analysis is to obtain a well-isolated photon peak in the M_X^2 spectrum (Fig. 7, histogram 5). The cuts necessary to reach this goal are described below.

First, standard acceptance cuts are applied in each arm. They use essentially the Hall A R functions [55], which are a way to handle complex cuts in a multidimensional space. In the R-function approach, the problem is transformed into the calculation, for each detected particle, of its "distances" to the acceptance boundaries and the combination of these distances into one single function. This R function takes continuous values: positive inside the acceptance domain, negative outside, and equal to zero on the boundaries. It can then be used

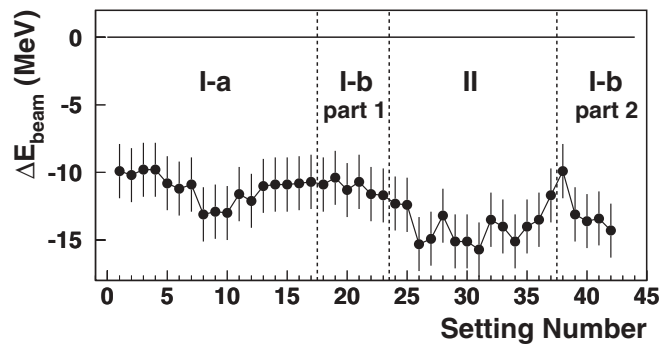

FIG. 6. The fitted offset in beam energy, ΔE_{beam}, versus the setting number (time ordered). There is one point per setting. The various data sets are delimited by the vertical lines. The horizontal line at $\Delta E_{\text{beam}} = 0$ corresponds to the nominal beam energy from the accelerator, $E_{\text{beam}} = 4.045$ GeV.

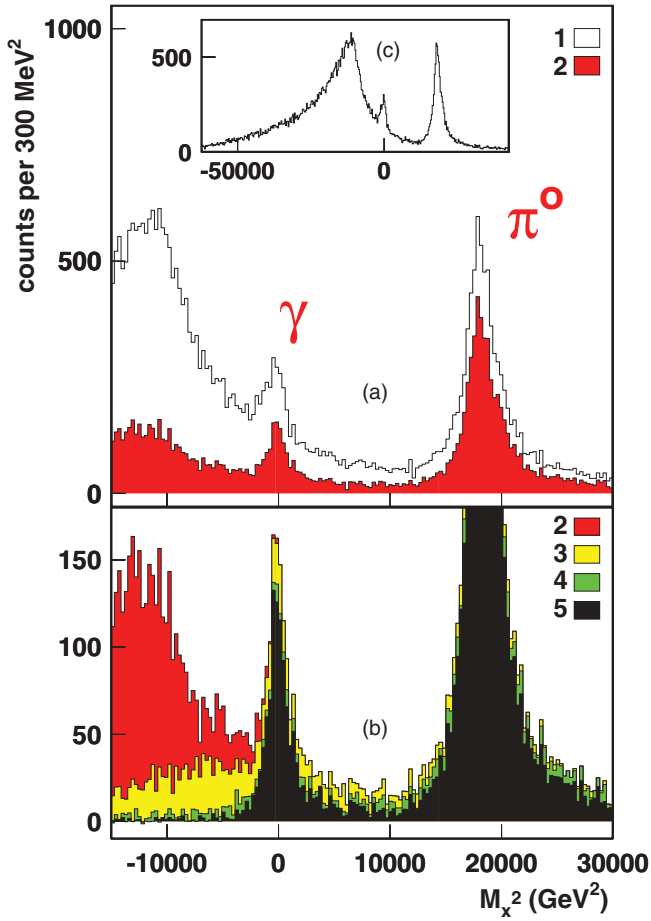

FIG. 7. (Color online) A sample of data set II: the experimental spectrum of the missing mass squared at various levels of cuts, added successively and labeled from 1 to 5. (a) The raw coincidences (1) and adding the R-function cut (2). (b) Adding the conditions $W > 0.96$ GeV (3), $Y_{\rm dif} < -0.012$ m (4), and $|x_{\rm dif}| < 3$ mm (5) (see the text for the description of the variables). Inset (c) shows histogram 1 in full scale abscissa.

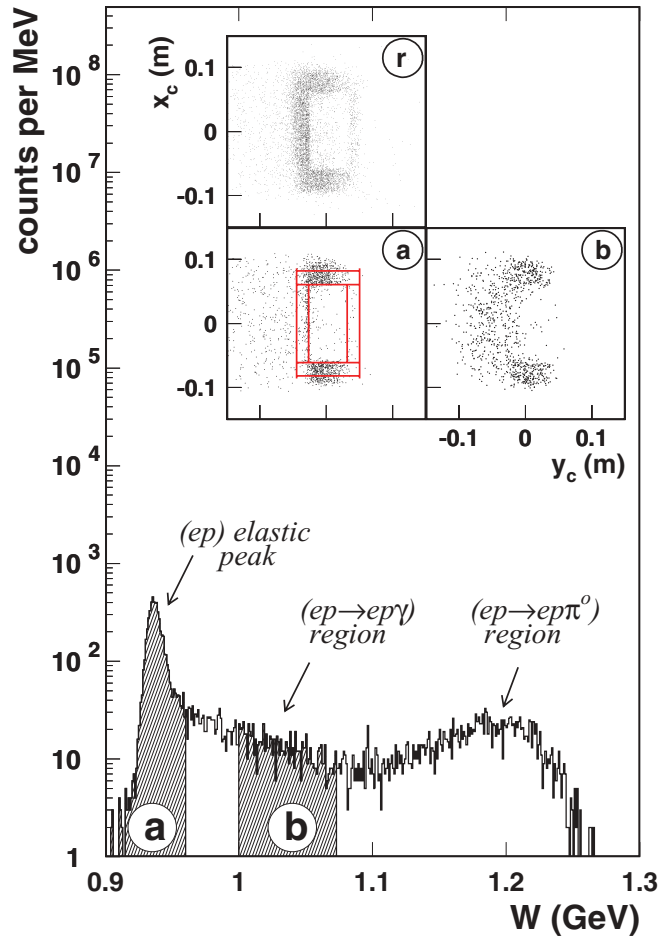

FIG. 8. (Color online) A sample of data set II: the experimental W spectrum for the coincidence events after the R-function cut. The insets show the proton impact in the HRS-H collimator calculated "elastically" (see text). Events in insets (a) and (b) correspond to the two hatched zones of the histogram: the ep elastic peak [$W < 0.96$ GeV (a)] and a typical VCS region [$1.0 < W < 1.073$ (b)]. In inset (a) a sketch of the tungsten collimator is drawn. The upper inset (r) shows the ep elastic events before applying the R-function cut.

as a one-dimensional cut (e.g., here we require R function >0). We also use additional—and largely redundant—contour cuts in two dimensions among the $(\delta, y, \theta, \varphi)_{\rm tg}$ quadruplet and restricted apertures in the plane of the entrance collimators. We note that the target endcaps, located at ± 75 mm on the beam axis, are not seen in coincidence, due to the rather large HRS-H spectrometer angles; so a cut in z_v is not necessary. The effect of the standard acceptance cuts is shown in Fig. 7 (histogram 2). Clearly they are not sufficient to fully clean the M_X^2 spectrum, and supplementary cuts are necessary.

Normally, the protons coming from ep elastic scattering are too energetic to be in the momentum acceptance of the HRS-H for our chosen settings. However, some of these protons go through the material of the entrance collimator (tungsten of 80 mm thickness), where they scatter and lose energy, after which they enter the acceptance and are detected. This problem cannot be avoided, since VCS near threshold is by nature close to ep elastic scattering.

As a result, a prominent ep elastic peak is seen in the W spectrum for true coincidences at the raw level and even after having applied the standard acceptance cuts, cf. Fig. 8. A striking evidence for "punch-through" protons is also provided by the insets in Fig. 8. These plots show the 2D impact point of the proton in the HRS-H collimator plane, calculated in a particular way. Here we do not use the information from the HRS-H; we only use the HRS-E information and the two-body ep elastic kinematics. Knowing the vertex point (from the HRS-E and the beam), the beam energy, and the scattered electron angles, one can deduce the point where the proton from ep elastic kinematics should have hit the collimator. This hit point is characterized by its coordinates x_c (vertical) and y_c (horizontal) in the HRS-H spectrometer frame. For events in the elastic peak of Fig. 8, the (x_c, y_c) distribution [inset 8(r)] reproduces faithfully the structure of the collimator material, proving that these are indeed protons punching through the

collimator. The R-function cut is able to remove part of these events but keeps the punching through the upper and lower parts of the collimator, as shown by inset 8(a). Of course, our purpose here is only illustrative; these events are not a concern, since they are removed by a simple cut in W around the elastic peak. The result of such a cut in terms of missing mass squared is displayed as histogram 3 of Fig. 7.

The main concern is that there are also "punch-through" protons at higher W, as evidenced by Fig. 8(b), where an image of the collimator material is still present. This region in W is the far radiative tail of the ep elastic process; in other words, it is the kinematical region of interest for VCS; therefore, one cannot use a cut in W. Nevertheless these "punch-through" events must be eliminated, because (i) they are badly reconstructed and (ii) the simulation cannot reproduce them (our simulation, which is used to obtain the cross section, see Secs. IV F and IV G, considers only perfectly absorbing collimators). To this aim, a more elaborate cut has been designed, which we now describe.

For a "punch-through" proton, the variables $(\delta, y, \theta, \varphi)_{\rm tg}$ obtained directly from the HRS-H are usually severely biased, due to the crossing of a thick collimator. Therefore, they are of little use, except for one particular combination, $y_{\rm collim}^{\rm Hadron} = y_{tg} + D\varphi_{\rm tg}$, where D is the distance from the target center to the collimator. This quantity $y_{\rm collim}^{\rm Hadron}$ gives the horizontal impact coordinate of the proton track in the collimator plane, as measured directly by the HRS-H. It is an unbiased variable, even for a "punch-through" proton. This is because the collimator plane is where the distortion happened. The reconstruction of the proton trajectory, which is performed backward, from focal plane to target, is correct down to the entrance collimator (and biased further down to the target). The idea is then to compare this quantity $y_{\rm collim}^{\rm Hadron}$ with the "elastic" coordinate y_c calculated just above. For "punch-through" protons the two calculations turn out to be in close agreement, hence, the difference $Y_{\rm dif} = y_c - y_{\rm collim}^{\rm Hadron}$ peaks at zero. We point out that this comparison can be done only for the horizontal coordinate, not in the vertical, due to the fact that the vertical extension $x_{\rm tg}$ is intrinsically not measured by the spectrometers.

Figure 9 shows the $Y_{\rm dif}$ distribution. Clean VCS events cover smoothly the $Y_{\rm dif} < 0$ region (dashed histogram), while experimental events (solid histogram) exhibit an extra-peak centered on zero. This peak corresponds to "punch-through" protons and is most efficiently eliminated by requiring the condition $Y_{\rm dif} < -12$ mm. The rejected events [inset 9(b)] again clearly reveal the image of the tungsten collimator. The retained events [inset 9(a)] show a smooth distribution in the (x_c, y_c) plane, well reproduced by the VCS simulation. The $Y_{\rm dif}$ cut is definitely efficient in isolating a clean photon peak, as shown by histogram 4 of Fig. 7.

Last, to obtain histogram 5 in Fig. 7 the geometrical variable $x_{\rm dif}$ (cf. Sec. IV C and Fig. 10) is selected around the central peak, i.e., in the interval $[-3,+3]$ mm, completing the removal of badly reconstructed events. It is worth noting that these two last cuts in $Y_{\rm dif}$ and $x_{\rm dif}$ (which are correlated but not equivalent) owe their efficiency to the excellent spectrometer intrinsic resolution in $y_{\rm tg}$, already emphasized in Sec. IV C.

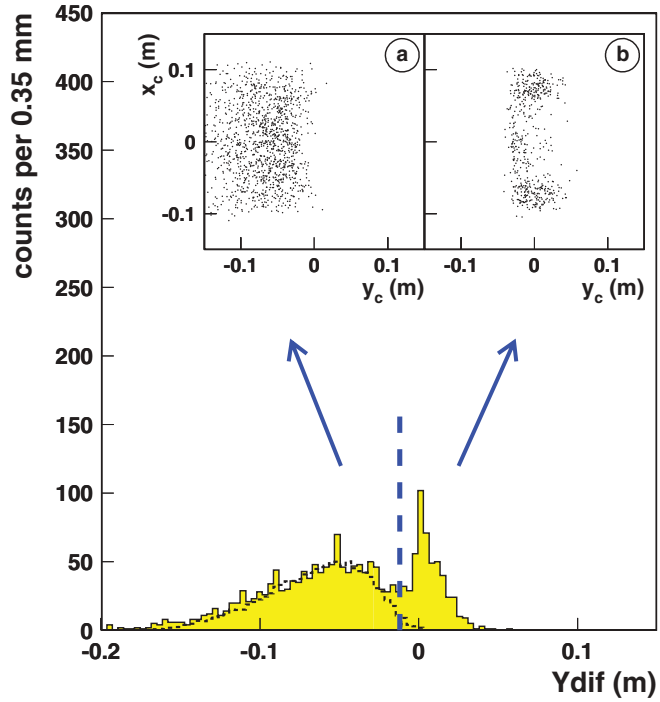

FIG. 9. (Color online) A sample of data set II: the experimental $Y_{\rm dif}$ spectrum (see text) for coincidence events surviving the application of the three following cuts simultaneously: R function > 0, $-5000 < M_X^2 < 5000$ MeV^2 and $W > 0.96$ GeV (solid histogram). The insets show the "elastically calculated" proton impact in the HRS-H collimator (see text) for $Y_{\rm dif} < -0.012$m [clean events (a)] and for $Y_{\rm dif} > -0.012$ m [punch-through protons (b)]. The dashed histogram corresponds to the VCS simulation with the same three cuts.

After the above cuts, a small fraction of events ($\leqslant 5\%$) still have more than one track in one arm or the other. The number of tracks is given by the VDC algorithm together with the parameters of the "golden track." One may either keep these multitrack events or reject them and renormalize the rate accordingly, based on the fact that these are still good events, just less clean. This second method was chosen, except for data set II, where the multitrack events are in very small proportion ($\leqslant 0.5\%$). Finally, events are selected in a window in M_X^2 around the photon peak, typically $[-5000,+5000]$ MeV^2, and in a certain W range. The lower bound in W corresponds to $q'_{\rm c.m.} = 30$ MeV/c and the upper bound is imposed depending on the type of analysis, LEX or DR (cf. Fig. 3). The (very few) random coincidences that remain are subtracted. After all cuts, the final event statistics for the analyses are about 35 000 (data set I-a), 13 000 (data set I-b), and 25 000 (data set II).

F. Monte Carlo simulation

The experimental acceptance is calculated by a dedicated Monte Carlo simulation which includes the actual beam configuration, target geometry, spectrometer acceptance, and resolution effects. It is described in detail in Ref. [56] and we recall here only the main features. The $ep \to ep\gamma$ kinematics are generated by sampling in the five variables

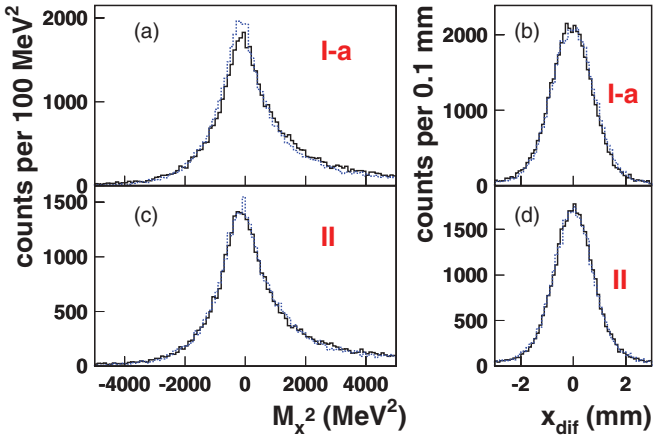

FIG. 10. (Color online) Data sets I-a (top) and II (bottom) after all cuts: comparison of experiment (solid histogram) and simulation (dotted histogram). [(a) and (c)] The missing mass squared in the VCS region; the peak full width at half maximum (FWHM) is about 1650 MeV^2. [(b) and (d)] The geometrical variable $x_{\rm dif}$ (see text); the peak FWHM is about 1.9 mm.

of the differential cross section $d^5\sigma/dk'_{\rm elab}d\Omega'_{\rm elab}d\Omega_{\gamma{\rm c.m.}}$. The scattered electron momentum and angles in the laboratory frame define the virtual photon, then with the angles of the Compton process in the CM one can build the complete three-body kinematics. Events are generated according to a realistic cross section, the (BH + Born) one, over a very large phase space. The emitted electron and proton are followed in the target materials, and the event is kept if both particles go through the [collimator + spectrometer] acceptance. One forms the four target variables $(\delta, y, \theta, \varphi)_{\rm tg}$ of each track and implements measurement errors on these variables in order to reproduce the resolution observed experimentally. Finally, one proceeds to the event reconstruction and analysis cuts in a way similar to the experiment.

As an example, Fig. 10 shows the distribution of the variables M_X^2 and $x_{\rm dif}$, for two VCS data sets after all cuts. These variables are not sensitive to the details of the physics; with an infinitely good resolution they should be δ functions. Therefore, they characterize the resolution achieved in the experiment. The agreement between the experimental and simulated data is very good not only in the main peak but also in the tails of the distributions, which is of importance as far as cuts are concerned. The excellent resolution achieved in missing mass squared allows us to cleanly separate the $(ep \to ep\gamma)$ and $(ep \to ep\pi^0)$ channels. The residual contamination of π^0 events under the γ peak is negligible for the settings analyzed here: Simulation studies show that it is smaller than 0.5%.

The radiative corrections are performed along the lines of Ref. [57], based on the exponentiation method. The simulation takes into account the internal and external bremsstrahlung of the electrons, because the associated correction depends on the acceptance and the analysis cuts. This allows the simulation to produce a realistic radiative tail in the M_X^2 spectrum, visible on the right side of the peak in Fig. 10 (left). The remaining part of the radiative effects, due to virtual corrections plus real corrections which do not depend on experimental cuts, is calculated analytically. It is found to be almost constant for the kinematics of the experiment [58], $F_{\rm rad} \simeq 0.93$; therefore, it is applied as a single numerical factor such that $d\sigma_{\rm corrected} = d\sigma_{\rm raw} \times F_{\rm rad}$ in each physics bin. The estimated uncertainty on $F_{\rm rad}$ is of the order of ± 0.02, i.e., it induces a $\pm 2\%$ uncertainty on the cross section, globally on each point and with the same sign.

G. Cross-section determination

We, first, explain the principle of the cross-section determination in a bin and then the chosen binning in phase space. In a given bin, after all cuts and corrections to the event rate, the analysis yields a number of experimental VCS events $N_{\rm exp}$ corresponding to a luminosity $\mathcal{L}_{\rm exp}$. Similarly, the simulation described in Sec. IV F yields a number of events $N_{\rm sim}$ corresponding to a luminosity $\mathcal{L}_{\rm sim}$. The experimental cross section is then obtained by

$$d^5\sigma^{\rm EXP} = \frac{N_{\rm exp}}{\mathcal{L}_{\rm exp}} \frac{\mathcal{L}_{\rm sim}}{N_{\rm sim}} d^5\sigma_{\rm sim}(P_0), \tag{8}$$

where the factor $[\mathcal{L}_{\rm sim} d^5\sigma_{\rm sim}(P_0)/N_{\rm sim}]^{-1}$ can be seen as an effective solid angle, or acceptance, computed by the Monte Carlo method. $d^5\sigma_{\rm sim}(P_0)$ is the cross section used in the simulation at a fixed point P_0 that can be chosen freely. As explained in Ref. [56], this method is justified when the shape of the cross section $d^5\sigma_{\rm sim}$ is realistic enough, and it gives rise to a measured cross section $(d^5\sigma/dk'_{\rm elab}d\Omega'_{\rm elab}d\Omega_{\gamma{\rm c.m.}})$ at some well-defined fixed points in phase space.

These points are defined by five independent variables. The most convenient choice with respect to the LET formulation is the set $(q_{\rm c.m.}, q'_{\rm c.m.}, \epsilon, \theta_{\rm c.m.}, \varphi)$. We will work at fixed $q_{\rm c.m.}$ and fixed ϵ and make bins in the other three variables. For the subsequent analyses, instead of the standard $(\theta_{\rm c.m.}, \varphi)$ angles, another convention $(\theta'_{\rm c.m.}, \varphi'_{\rm c.m.})$ is chosen. It is deduced from the standard one by a simple rotation: The polar axis for $\theta'_{\rm c.m.}$ is chosen perpendicularly to the lepton plane, instead of being aligned with the $\vec{q}_{\rm c.m.}$ vector (see Appendix A for more details). This new system of axis allows an angular binning in which the direction of $\vec{q}_{\rm c.m.}$ does not play a privileged role. Due to the narrow proton cone in the laboratory, the angular acceptance in the CM is almost complete for data sets I-a and II. This is illustrated in Fig. 11. We note that the two peaks of the BH cross section, located in-plane, are out of the acceptance (see also Fig. 12). This is on purpose, since in these peaks the polarizability effect in the cross section vanishes. When W increases, the acceptance reduces to more backward-scattering angles [6].

Table X in Appendix A summarizes the bin sizes and the chosen fixed points in phase space. As a consequence, the results of the experiment are obtained at two fixed values of Q^2: 0.92 and 1.76 GeV^2.

In Eq. (8) the cross section $d^5\sigma^{\rm EXP}$ is, first, calculated using the BH + Born cross section for $d^5\sigma_{\rm sim}$, i.e., no polarizability effect is included in the simulation. Then, to improve the accuracy, we include a Non-Born term in $d^5\sigma_{\rm sim}$, based on what we find for the polarizabilities at the previous iteration.

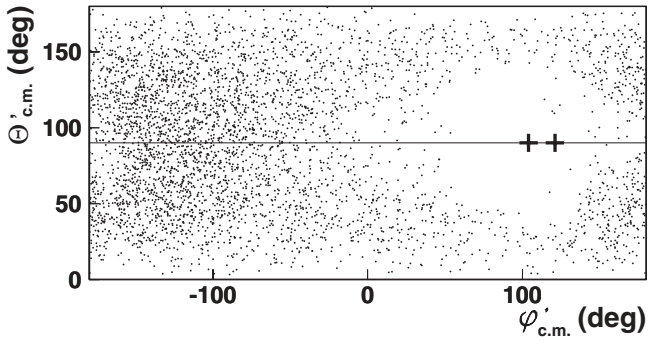

FIG. 11. Accepted phase space in $(\theta'_{\text{c.m.}}, \varphi'_{\text{c.m.}})$ for data set I-a. The two crosses denote the position of the BH peaks and the horizontal line corresponds to in-plane kinematics ($\theta'_{\text{c.m.}} = 90^\circ$ or $\varphi = 0^\circ$ and 180°).

Below the pion threshold this Non-Born term is the first-order LEX term of Eq. (2). For the region above the pion threshold, this Non-Born term is computed using the dispersion relation formalism, and the iterations are made on the free parameters of the model. In all cases this iterative procedure shows good convergence.

H. Sources of systematic errors

The systematic errors on the cross section come from three main sources: (1) overall absolute normalization, (2) beam energy, and (3) horizontal angles of the detected particles.

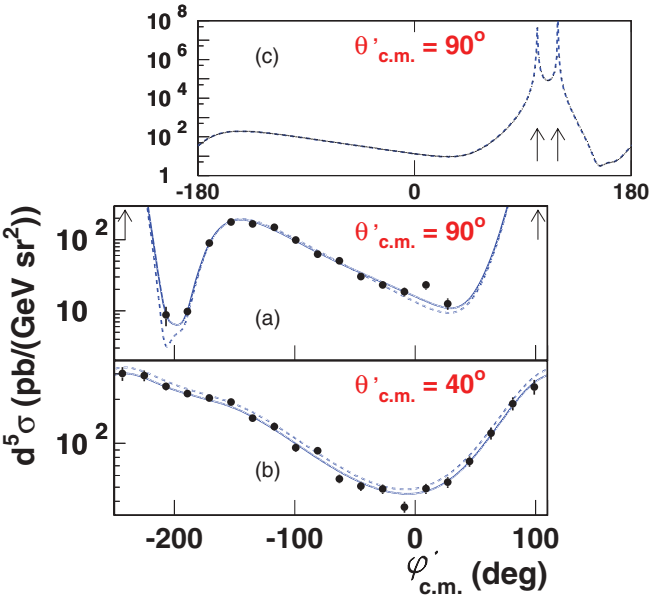

FIG. 12. (Color online) Data set I-a below the pion threshold at $q'_{\text{c.m.}} = 105$ MeV/c. The $(ep \to ep\gamma)$ cross section is shown in-plane $[\theta'_{\text{c.m.}} = 90^\circ$, (a)] and out-of-plane $[\theta'_{\text{c.m.}} = 40^\circ$, (b)]. The dotted curve is the BH + Born calculation. The solid curve includes the first-order GP effect calculated using our measured structure functions. The errors on the points are statistical only, as well as in the six next figures. The upper plot (c) shows the in-plane BH + Born cross section with a full-scale ordinate and the more traditional abscissa running between $\varphi'_{\text{c.m.}} = -180^\circ$ and $\varphi'_{\text{c.m.}} = +180^\circ$.

The uncertainty in the absolute normalization has principally three origins: the radiative corrections known to ±2%, the experimental luminosity known to ±1%, and the detector efficiency corrections known to ±0.5% (see previous sections). Added in quadrature, they give a overall normalization error of ±2.3%, applying to all cross-section points with the same sign.

The uncertainty in the beam energy, deduced from the offsets study of Sec. IV D, is taken equal to ±2 MeV. The uncertainty in horizontal angles essentially reflects the accuracy of the optic tensors and is taken equal to ±0.5 mr in each arm. To study the systematic error induced by the beam energy or the horizontal angles, the experimental events are re-analyzed with these parameters changed, one by one separately, by one standard deviation. One obtains in each case a set of modified cross-section data; in certain cases we observe a change of shape of the cross section. One can summarize these effects by saying that error sources (2) and (3) taken together are equivalent to an average systematic uncertainty of ±6% (respectively, ±7%) on the cross section for data set I-a (respectively, data set II). These errors include substantial point-to-point correlations.

Systematic errors on the physics observables will be discussed in Secs. V B1 and V B2.

I. Choice of proton form factors

The proton elastic form factors G_E^p and G_M^p are an important input in an analysis of VCS at low energy. Indeed, they are needed to calculate the BH + Born cross section, which is at the basis of the low-energy expansion. Throughout these analyses the form factor parametrization of Brash *et al.* [59] was chosen. It provided the first fit consistent with the observed departure from one of the ratio $\mu_p G_E^p / G_M^p$ in our Q^2 range [60,61].

The VCS structure functions and GPs are always extracted by measuring a *deviation* from the BH + Born process—either analytically as in the LEX approach or in a more complex way as in the DR approach. This statement means that the GP extraction is sensitive to both cross sections, $d^5\sigma^{\text{EXP}}$ and $d^5\sigma^{\text{BH+Born}}$: A 1% change on $d^5\sigma^{\text{EXP}}$ has the same impact as a 1% change on $d^5\sigma^{\text{BH+Born}}$. This last cross section is not known with an infinite accuracy, due to uncertainties on the proton form factors. Therefore, a systematic error should be attached to our calculation of $d^5\sigma^{\text{BH+Born}}$. To treat it in a simplified way, we consider that form factor uncertainties are equivalent to a global scale uncertainty of ±2% on $d^5\sigma^{\text{BH+Born}}$. Then, when dealing with the extraction of the physics observables (Secs. V B and V C), this effect can be put instead on $d^5\sigma^{\text{EXP}}$, i.e., it can be absorbed in the overall normalization uncertainty of the experiment. Consequently, in Secs. V B and V C, we will simply enlarge the systematic error due to normalization (source 1 in Sec. IV H) from ±2.3% to ±3% (= quadratic sum of 2.3% and 2%).

V. RESULTS AND DISCUSSION

We, first, present the results for the photon electroproduction cross section. The VCS structure functions and the GPs

TABLE V. The structure functions obtained by the LEX analysis. The first error is statistical, the second one is the total systematic error. The reduced χ^2 of the fit and the number of degrees of freedom are also given.

This experiment, LEX analyses				
Data set	Q^2 (GeV^2)	ϵ	$P_{LL} - P_{TT}/\epsilon$ (GeV^{-2})	P_{LT} (GeV^{-2})
I-a	0.92	0.95	$1.77 \pm 0.24 \pm 0.70$	$-0.56 \pm 0.12 \pm 0.17$
II	1.76	0.88	$0.54 \pm 0.09 \pm 0.20$	$-0.04 \pm 0.05 \pm 0.06$
I-a	$\chi^2_{\min} = 1.22$ for 32 DOF			
II	$\chi^2_{\min} = 1.50$ for 31 DOF			

then are presented and discussed. The main results for these observables are contained in Tables V, VII, and IX.

A. The $ep \to epy$ cross section

The experiment described here provides a unique set of data for VCS studies, combining altogether a large angular phase space (including out-of-plane angles), a large domain in CM energy (from the threshold to the Δ resonance), and an access to the high-Q^2 region. Our cross-section data are reported in Tables XIII–XVII of Appendix C.

1. Angular and energy dependence

Selected samples of our results are presented in Figs. 12–15. Figure 12 shows the measured cross section for the highest value of $q'_{\text{c.m.}}$ below the pion threshold (105 MeV/c). The in-plane cross section ($\theta'_{\text{c.m.}} = 90^\circ$) rises by seven orders of magnitude in the vicinity of the BH peaks, which are indicated by the two arrows. The out-of-plane cross section has a much smoother variation. As expected, the measured values exhibit a slight departure from the BH + Born calculation, due to the polarizabilities. The magnitude of this effect is best seen in Fig. 13, which depicts the deviation of the measured cross section relative to BH + Born: in-plane this ratio varies between -5% and $+20\%$, except in the dip near $\varphi'_{\text{c.m.}} = -200^\circ$ (or $+160^\circ$), where it reaches larger values. This complex pattern is due to the VCS-BH interference.

TABLE VI. The fitted dipole mass parameters Λ_α and Λ_β for the three independent data sets. The first and second errors are statistical and total systematic, respectively. The reduced χ^2 of the fit and the number of degrees of freedom are also given.

Data set	Λ_α (GeV)	Λ_β (GeV)
I-a	$0.741 \pm 0.040 \pm 0.175$	$0.788 \pm 0.041 \pm 0.114$
I-b	$0.702 \pm 0.035 \pm 0.037$	$0.632 \pm 0.036 \pm 0.023$
II	$0.774 \pm 0.050 \pm 0.149$	$0.698 \pm 0.042 \pm 0.077$
I-a	$\chi^2_{\min} = 1.49$ for 164 DOF	
I-b	$\chi^2_{\min} = 1.34$ for 328 DOF	
II	$\chi^2_{\min} = 1.31$ for 151 DOF	

TABLE VII. The VCS structure functions obtained by the DR analysis. The first error is statistical, the second one is the total systematic error.

This experiment, DR analysis				
Data set	Q^2 (GeV^2)	ϵ	$P_{LL} - P_{TT}/\epsilon$ (GeV^{-2})	P_{LT} (GeV^{-2})
I-a	0.92	0.95	$1.70 \pm 0.21 \pm 0.89$	$-0.36 \pm 0.10 \pm 0.27$
I-b	0.92	0.95	$1.50 \pm 0.18 \pm 0.19$	$-0.71 \pm 0.07 \pm 0.05$
II	1.76	0.88	$0.40 \pm 0.05 \pm 0.16$	$-0.09 \pm 0.02 \pm 0.03$

Out-of-plane the polarizability effect is much more uniform, with an average value of $\sim -10\%$.

Another selected sample of results is displayed in Fig. 14, this time above the pion threshold (at $q'_{\text{c.m.}} = 215$ MeV/c) and for backward angles of the outgoing photon. There, the first-order term of the LET becomes clearly insufficient to explain the observed cross section, while the calculation of the DR model, which includes all orders, performs quite well. The energy dependence of the cross section, i.e., the dependence in $q'_{\text{c.m.}}$ or W, is governed by a strong rise when $q'_{\text{c.m.}}$ tends to zero due to the vicinity of the ep elastic scattering and a resonant structure in the region of the $\Delta(1232)$. These features can be seen in Fig. 18.

2. Overall normalization test

The effect of the GPs in the photon electroproduction cross section roughly scales with the outgoing photon energy $q'_{\text{c.m.}}$. Therefore, the physics results are determined essentially from the bins at high $q'_{\text{c.m.}}$, which have the highest sensitivity to the GPs. At our lowest $q'_{\text{c.m.}}$ of 45 MeV/c, this sensitivity is much reduced, and one can test another aspect of the experiment, namely the overall normalization.

When $q'_{\text{c.m.}}$ tends to zero, $d^5\sigma^{\text{EXP}}$ formally tends to the known BH + Born cross section. This is a model-independent statement, best illustrated by the LEX expansion of Eq. (2). At $q'_{\text{c.m.}} = 45$ MeV/c, the first-order term ($q'_{\text{c.m.}}\phi\Psi_0$), calculated using our measured values for the structure functions, is very small. It is about 2% of the BH + Born cross section, and it remains essentially unchanged when the structure functions are varied by one standard deviation. Therefore, at the lowest $q'_{\text{c.m.}}$ the comparison of the measured cross section $d\sigma^{\text{EXP}}$ with the cross section $d^5\sigma^{\text{calc}}$ calculated from Eq. (2),

$$d^5\sigma^{\text{calc}} = d^5\sigma^{\text{BH+Born}} + q'_{\text{c.m.}}\phi\Psi_0,$$

TABLE VIII. Our result for the P_{LL} structure function from the DR analysis. The value of P_{TT} is the parameter-free DR prediction.

Data set	Q^2 (GeV^2)	P_{LL} (exp.) (GeV^{-2})	P_{TT} (theory) (GeV^{-2})
I-a	0.92	$1.19 \pm 0.21 \pm 0.89$	-0.485
I-b	0.92	$0.99 \pm 0.18 \pm 0.19$	-0.485
II	1.76	$0.24 \pm 0.05 \pm 0.16$	-0.142

TABLE IX. The electric and magnetic GPs extracted in this experiment at $Q^2 = 0.92$ GeV^2 and 1.76 GeV^2. The first error is statistical. The second one is the total systematic error, obtained by propagating the errors on $(\Lambda_\alpha, \Lambda_\beta)$ of Table VII (for the DR analysis) or the errors on the structure functions of Table V (for the LEX analysis).

Data set	Q^2 (GeV^2)	$\alpha_E(Q^2)$ (10^{-4} fm^3)	$\beta_M(Q^2)$ (10^{-4} fm^3)
		DR analysis	
I-a	0.92	$1.02 \pm 0.18 \pm 0.77$	$0.13 \pm 0.15 \pm 0.42$
I-b	0.92	$0.85 \pm 0.15 \pm 0.16$	$0.66 \pm 0.11 \pm 0.07$
II	1.76	$0.52 \pm 0.12 \pm 0.35$	$0.10 \pm 0.07 \pm 0.12$
		LEX analysis+[spin part subtraction by DR]	
I-a	0.92	$1.09 \pm 0.21 \pm 0.60$	$0.42 \pm 0.18 \pm 0.26$
II	1.76	$0.82 \pm 0.20 \pm 0.44$	$-0.06 \pm 0.17 \pm 0.20$

is essentially a test of the absolute normalization of the experiment. In practice, one allows $d\sigma^{\rm EXP}$ to be renormalized by a free factor $F_{\rm norm}$, and a χ^2 is minimized between $d\sigma^{\rm EXP}$ and $d\sigma^{\rm calc}$ as a function of $F_{\rm norm}$. The test is performed on data sets I-a and II at the lowest $q'_{\rm c.m.}$; the $\chi^2_{\rm min}$ is always found for $F_{\rm norm}$ in the range [0.99, 1.01]. An example is given in Fig. 15. To conclude, our cross-section data need very little renormalization, less than 1%. This means in particular that there is a good consistency between the chosen parametrization of the proton form factors and the way the radiative corrections are applied to the experiment.

B. The VCS structure functions

As mentioned in Sec. II, the VCS structure functions and the GPs do not enter the $ep \to ep\gamma$ cross section in the most straightforward way. A theoretical tool is needed to extract them from the experiment. The structure functions have been extracted by two different methods: the LEX analysis and the DR analysis. This section presents the methods, the results, and a discussion.

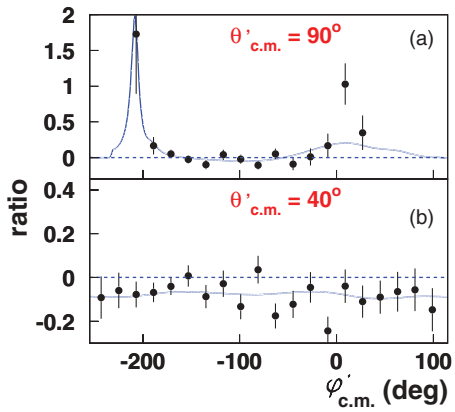

FIG. 13. (Color online) The ratio $(d\sigma^{\rm EXP} - d\sigma^{\rm BH+Born})/d\sigma^{\rm BH+Born}$ for the data points of the previous figure. The solid curve shows the first-order GP effect calculated using our measured structure functions.

1. LEX analysis

This analysis is based on the method described in Sec. II C. It is performed on the data sets I-a and II separately. An upper cut in W is imposed [$W < (m_p + m_{\pi^0})$ or $q'_{\rm c.m.} < 126\,{\rm MeV}/c$] to stay below the pion threshold. The LEX analysis uses the cross-section data of Tables XIII and XIV only.

For each measured point in $(q'_{\rm c.m.}, \theta'_{\rm c.m.}, \varphi'_{\rm c.m.})$, one forms the quantity

$$\Delta\mathcal{M} = (d^5\sigma^{\rm EXP} - d^5\sigma^{\rm BH+Born}) / (q'_{\rm c.m.}\phi). \qquad (9)$$

The Ψ_0 term of Eq. (2) is the extrapolation of $\Delta\mathcal{M}$ to $q'_{\rm c.m.} = 0$ in each bin in $(\theta'_{\rm c.m.}, \varphi'_{\rm c.m.})$. Below the pion threshold, our $\Delta\mathcal{M}$ data do not exhibit any significant $q'_{\rm c.m.}$ dependence within error bars. An example is shown in Fig. 16. The extrapolation to $q'_{\rm c.m.} = 0$ is, thus, done simply by averaging $\Delta\mathcal{M}$ over the points at $q'_{\rm c.m.} = 45$, 75, and 105 MeV/c. This is equivalent to neglecting the higher-order terms $O(q'^2_{\rm c.m.})$ in this $q'_{\rm c.m.}$ range.

A linear fit of the Ψ_0 points, based on Eq. (3), then yields the two structure functions $P_{LL} - P_{TT}/\epsilon$ and P_{LT}. At fixed $q_{\rm c.m.}$ and ϵ, the coefficients v_1 and v_2 depend only on the Compton

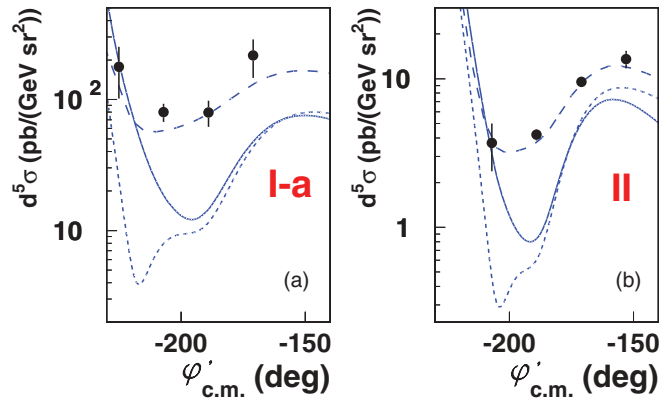

FIG. 14. (Color online) The $(ep \to ep\gamma)$ cross section for data sets I-a (a) and II (b) at $q'_{\rm c.m.} = 215\,{\rm MeV}/c$, in-plane ($\theta'_{\rm c.m.} = 90^\circ$) as a function of $\varphi'_{\rm c.m.}$. The dashed curve is the DR model calculation, with parameter values as fitted in the experiment. The dotted (respectively, solid) curve is the BH + Born cross section (respectively, plus a first-order GP effect).

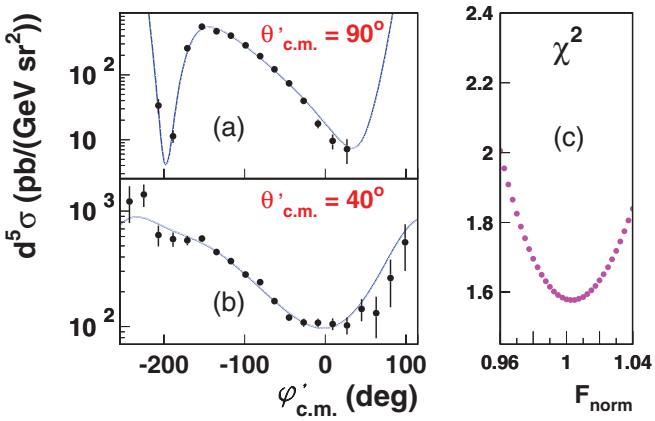

FIG. 15. (Color online) Data set I-a. The $(ep \to ep\gamma)$ cross section at the lowest $q'_{\rm c.m.}$ of 45 MeV/c, for in-plane (a) and out-of-plane (b) kinematics. The solid curve is the (BH + Born + first-order GP) cross section. The right plot (c) shows the reduced χ^2 of the normalization test.

angles $(\theta'_{\rm c.m.}, \varphi'_{\rm c.m.})$. The good lever arm in v_1 and v_2 is provided by the large coverage in these two angles. Figure 17 represents the fit in terms of Ψ_0/v_2 versus the ratio v_1/v_2. P_{LT} is given by the intercept and $P_{LL} - P_{TT}/\epsilon$ by the slope of the straight line fit. The rather good χ^2 (cf. Table V) confirms that higher-order terms $O(q'^2_{\rm c.m.})$ are small below the pion threshold. The values obtained for the two structure functions with their errors are reported in Table V.

The statistical errors are provided by the χ^2 minimization. The fit can be performed on out-of-plane and in-plane data separately: The two corresponding types of results agree within statistical errors for data set I-a but only within total errors (statistical + systematic) for data set II.

For the systematic errors on the structure functions, one proceeds as for the cross section. The same sources of uncertainty are considered: (1) overall absolute normalization, (2) beam energy, and (3) horizontal angles of the detected particles. The only difference is that the normalization error is now enlarged to ±3% to account for uncertainties in the proton form factors, as explained in Sec. IV I. The LEX analysis is redone using several sets of modified cross-section data, as described in Sec. IV H. The deviations of the structure functions with respect to the nominal analysis are recorded for all these cases and, finally, added in quadrature. Detailed contributions to the systematic error are given in Table XI of Appendix B. A number of complementary systematic checks were performed, e.g., by changing the analysis cuts or the phase-space points for the cross section. The physics results obtained in these studies all stay within the systematic error bars of Table V.

2. DR analysis

This analysis is based on the DR formalism introduced in Sec. II D. It is applied to the three data sets I-a, I-b, and II separately. The restriction to stay below the pion threshold is now removed. Strictly speaking, the DR formalism provides a rigorous treatment of the VCS amplitude only up to the two-pion threshold ($W = 1.21$ GeV). However, the two-pion contribution is still small just above threshold; the upper limit in W in our analysis is taken at $W = 1.28$ GeV, considering that the model calculation is able to describe the experimental data in this energy range (see, for example, Fig. 3 of Ref. [6]). The cross-section data of Tables XIII to XVII are included. Globally, two different domains in W are involved: (1) the region of the $\Delta(1232)$ resonance for data set I-b and (2) the region essentially below the pion threshold, with a small extension above, for data sets I-a and II (cf. Fig. 3).

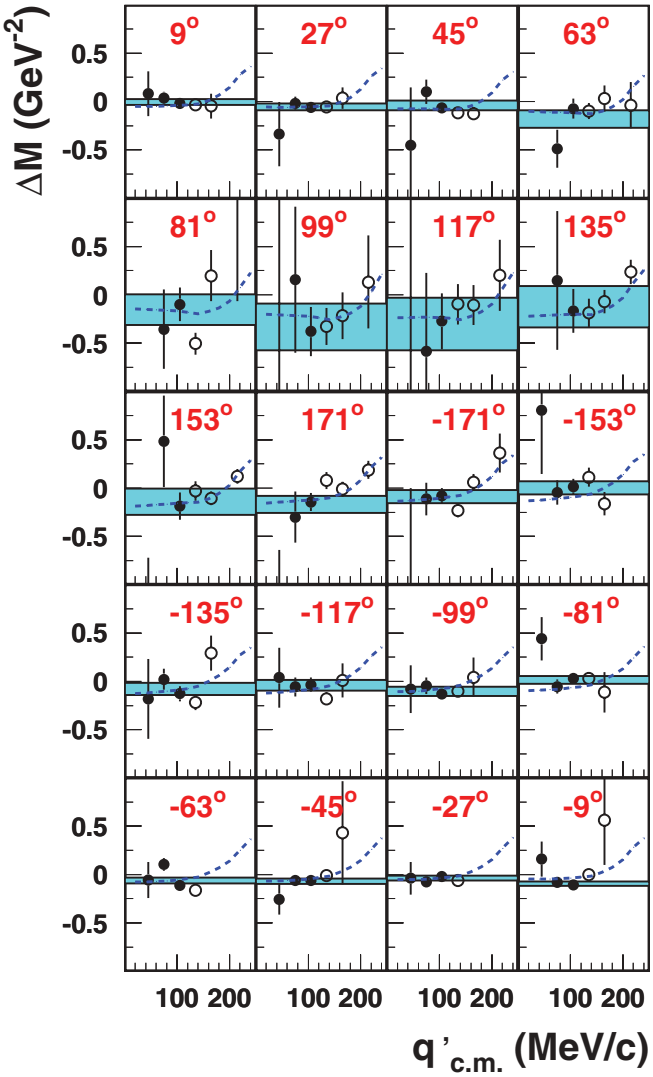

FIG. 16. (Color online) The $q'_{\rm c.m.}$ dependence of the quantity $\Delta\mathcal{M}$ [see Eq. (9)] in each angular bin. Example of data set I-a at $\theta'_{\rm c.m.} = 40°$ (out-of-plane). The value of $\varphi'_{\rm c.m.}$ is written in each plot. The shaded band is the result of the LEX fit, "ΔM = const," within $\pm 1\sigma$ error (statistical). The fit is performed on the three points below the pion threshold (solid circles). The other points (open circles) are above the pion threshold and do not participate to the LEX fit. The dashed curve shows the calculation of $\Delta\mathcal{M}$ by use of the DR model, using the results of our DR fit (see Sec. V B2) which is performed on all points (solid + open circles).

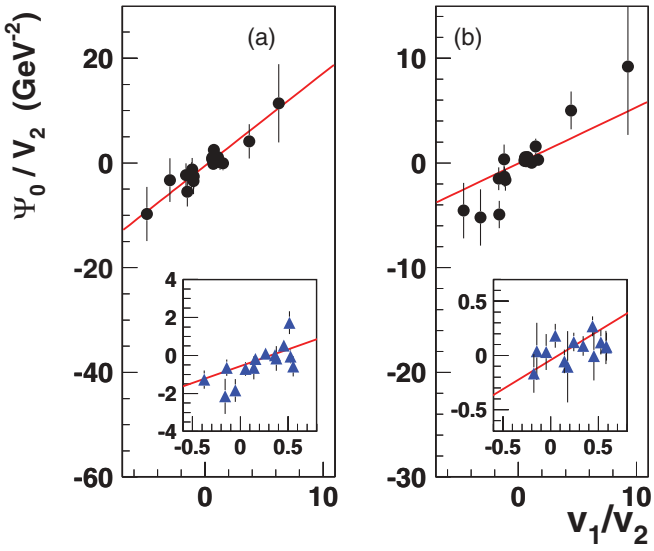

FIG. 17. (Color online) A graphical representation of the LEX fit for data sets I-a (a) and II (b). Each point in v_1/v_2 corresponds to a different bin in $(\theta'_{\text{c.m.}}, \varphi'_{\text{c.m.}})$. The solid circles correspond to out-of-plane data. The inset in plots (a) and (b) is a close-up of the in-plane data (triangles), all concentrated at small values of v_1/v_2. The straight line refers to the fit performed on all data points (in-plane + out-of-plane).

Some of our cross-section measurements above the pion threshold are depicted in Figs. 14 and 18. Figure 18 clearly shows the excitation of the $\Delta(1232)$ resonance. The DR model gives a good description of the data and the various curves illustrate the sensitivity to the model parameters. The peak position is located at a lower mass than the Δ mass, a feature due to the VCS-BH interference. Figure 16 shows how the DR

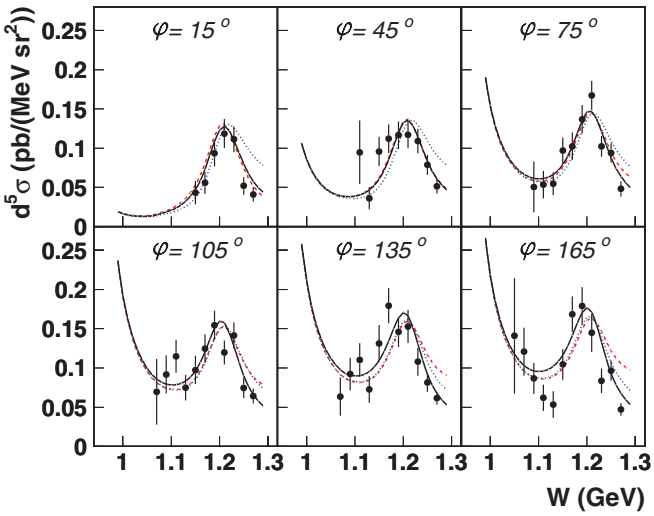

FIG. 18. (Color online) Data set I-b. The $(ep \to ep\gamma)$ cross section at fixed $\cos\theta_{\text{c.m.}} = -0.975$ and six bins in φ (from Table XVII). The curves show the DR model calculation for parameter values $(\Lambda_\alpha, \Lambda_\beta) = (0.70, 0.63)$ GeV (solid line), (1.20, 0.63) GeV (dashed line), (0.70, 1.00) GeV (dotted line).

model reproduces the $q'_{\text{c.m.}}$ dependence of the quantity $\Delta\mathcal{M}$ introduced in Sec. V B1: The flat behavior below the pion threshold is followed by a rise near the Δ resonance, where the higher-order terms become dominant.

The DR formalism incorporates the BH + Born cross section and a Non-Born part which contains the free parameters Λ_α and Λ_β (cf. Sec. II D). The analysis method consists in fitting these two parameters by a χ^2 minimization (called the "DR fit") which compares the model cross section to the measured one. The minimization cannot be solved analytically; the χ^2 is computed on the nodes of a grid in $(\Lambda_\alpha, \Lambda_\beta)$ and its minimum is found numerically. For each data set a clear and single minimum is found, with a reasonable χ^2_{min} value. The fitted values for $(\Lambda_\alpha, \Lambda_\beta)$ corresponding to our three independent data sets are reported in Table VI.

The statistical errors on $(\Lambda_\alpha, \Lambda_\beta)$ are given by the standard error ellipse at $(\chi^2_{\text{min}} + 1)$. The systematic errors are treated exactly as in the LEX method, i.e., by finding the solution in $(\Lambda_\alpha, \Lambda_\beta)$ for modified cross-section sets and summing quadratically the resulting variations with respect to the nominal analysis. Table XII of Appendix B gives these detailed contributions. One will note that the systematic errors appear to be much smaller in the case of data set I-b. This may come from the different phase-space coverage of this data set (in $\theta_{\text{c.m.}}$ and W), inducing a different sensitivity to the sources of errors. Remarkably, all our fitted values of the $(\Lambda_\alpha, \Lambda_\beta)$ parameters lie in a narrow range, [0.63,0.79] GeV, indicating that the asymptotic part of the GPs [$\Delta\alpha$, $\Delta\beta$ of Eqs. (6) and (7)] behaves roughly as a single dipole in the Q^2 range of 1–2 GeV^2.

Once we have the fitted values of Λ_α and Λ_β, the DR model is able to calculate the scalar GPs and the scalar part of the structure functions [defined in Eq. (4)] at the Q^2 under consideration. The full structure functions $P_{LL} - P_{TT}/\epsilon$ and P_{LT} are then formed by adding the spin part. This last part is parameter free, since all spin GPs are fixed in the DR model. The complete DR calculation is done separately for each data set using the inputs of Table VI. The results for $P_{LL} - P_{TT}/\epsilon$ and P_{LT} are given in Table VII. The results for P_{LL} alone are given in Table VIII, where we have also reported the DR value of the spin part P_{TT}.

To obtain the statistical and systematic errors in Tables VII and VIII, the errors on $(\Lambda_\alpha, \Lambda_\beta)$ are propagated to the structure functions, using the model calculation. One will note that the DR model exists in several versions, each one using a different set of MAID multipoles for pion electroproduction. Our analyses were done using MAID 2000. With more recent multipole sets (MAID 2003 or 2007), the $(ep \to ep\gamma)$ cross section in the DR model changes by ∼1–2% in our kinematics. Therefore, the results presented here are not expected to change noticeably with the version update; they should stay largely within the quoted statistical error.

3. *Consistency between the different analyses*

The consistency between the two types of analysis, LEX and DR, can be tested only on $P_{LL} - P_{TT}/\epsilon$ and P_{LT} (not on the GPs themselves), because these two structure functions are the only direct outcome of the LEX analysis. In Fig. 19

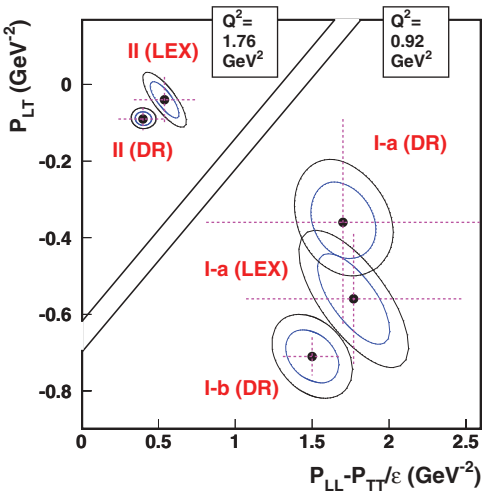

FIG. 19. (Color online) The structure functions obtained by the two methods (LEX and DR) at $Q^2 = 0.92$ GeV^2 and 1.76 GeV^2. Each Q^2 corresponds to a solid-line polygon as marked. For each point, the inner ellipse is the contour at $(\chi^2_{\min} + 1)$, yielding the standard deviation on each structure function independently. The outer ellipse at $(\chi^2_{\min} + 2.3)$ corresponds to a probability of 68% that both structure functions are inside the contour simultaneously. The statistical errors quoted in Tables V and VII are given by the boundaries of the inner contour. Dotted crosses give the size of the systematic error.

we give a comprehensive view of all our measurements of the structure functions, for the three independent data sets and the two analysis methods. The representation in the form of standard error ellipses indicates that error correlations between the two structure functions are larger in the LEX case than in the DR case.

At $Q^2 = 0.92$ GeV^2, the three measurements of $P_{LL} - P_{TT}/\epsilon$ agree very well. The agreement is less good on the three values of P_{LT}, in particular between the separate DR extractions of P_{LT} from data sets I-a and I-b, i.e., essentially below and above the pion threshold. However, these values become compatible within total errors, including systematics. As a side remark, we note that a single DR analysis on the whole W range would be possible, by joining together data sets I-a and I-b, but it would mask these different results for P_{LT}. At $Q^2 = 1.76$ GeV^2, the LEX and DR results are in mild agreement.

Overall, Fig. 19 shows a rather good consistency between the two types of extraction methods, LEX and DR, at each Q^2. We also point out that the systematic error generally dominates in our physics results (data sets I-a and II). This feature can be understood already at the cross-section level, where the size of the systematic error (∼7% of the cross section) is about half the size of the expected GP effect (10–15% of the cross section below the pion threshold).

At one given Q^2, our LEX and DR results are obtained in most cases from nonindependent, partially overlapping data sets. Therefore, we do not propose any averaging of the points shown in Fig. 19 at each Q^2. Only the I-b(DR) and I-a(DR) results are truly independent and could possibly be averaged.

4. Q^2 dependence of the structure functions

Most of the theoretical models for GPs (Sec. II B) have a validity domain limited to low energies and low Q^2. At Q^2 values of 1–2 GeV^2, the only relevant confrontation of experimental data is with the dispersive approach, so we will focus on this model. ChPT will still be included as a reference in the lower-Q^2 region.

Figure 20 shows the structure functions obtained in this experiment, together with the other existing measurements and model calculations. The main strength of the JLab data is to have enlarged considerably the measured Q^2 range, allowing us to put in perspective different regions of four-momentum transfer, "high" and "low."

The experimental data follow the global trend of the models, i.e., a more or less continuous falloff for $P_{LL} - P_{TT}/\epsilon$, and

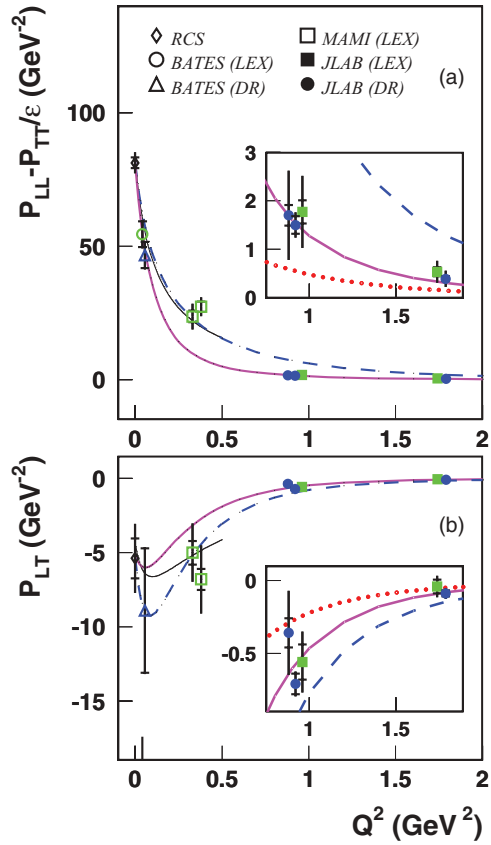

FIG. 20. (Color online) The structure functions $P_{LL} - P_{TT}/\epsilon$ (a) and P_{LT} (b) measured at Bates [8], MAMI [1,3], and JLab [5] (this experiment). The RCS point deduced from Ref. [17] is also included. The insets are a close-up the Q^2 region of this experiment. Some points are slightly shifted in the abscissa for visibility. The inner (outer) error bar on the points is statistical (total). The thin solid curve is the HBChPT calculation [27]. The other curves show DR calculations [32] performed with various sets of parameters. (a) $\Lambda_\alpha = 0.7$ GeV (thick solid line) and $\Lambda_\alpha = 1.79$ GeV (dashed line). (b) $\Lambda_\beta = 0.7$ GeV (thick solid line) and $\Lambda_\beta = 0.5$ GeV (dashed line). $\epsilon = 0.9$ is chosen to draw the curves for $P_{LL} - P_{TT}/\epsilon$. The dotted curve in the insets is the spin part as given by the DR model: $-P_{TT}/0.9$ (upper) and P_{LTspin} (bottom).

for P_{LT} a rather flat behavior in the low-Q^2 region followed by an asymptotic trend to zero. At low Q^2 the data are in good agreement with HBChPT at $O(p^3)$ [27] (thin solid curve). The DR model does not give a parameter-free prediction of $P_{LL} - P_{TT}/\epsilon$ and P_{LT}. To draw the DR curves in Fig. 20 we have fixed the dipole mass parameters Λ_α and Λ_β of Eqs. (6) and (7) and, further, assumed that they are constant versus Q^2. This is a simplification, aiming only at a simple graphical representation; as explained in Sec. II D, the DR model has no such constraint intrinsically. The solid curve shows the DR calculation for typical parameter values obtained in our experiment, $\Lambda_\alpha = \Lambda_\beta = 0.7$ GeV. The dashed curve shows the DR calculation for other parameter values, which agree better with some of the low-Q^2 data.

As a general statement, there is no such single DR curve which goes well through all the data points over the whole Q^2 range. It means that a single dipole function for the unconstrained parts $\Delta\alpha$ and $\Delta\beta$ of Eqs. (6) and (7) is too limiting. This is especially true for the first structure function $P_{LL} - P_{TT}/\epsilon$: All measurements are compatible with the thick solid curve ($\Lambda_\alpha = 0.70$ GeV), except near $Q^2 \simeq 0.3$ GeV^2 (MAMI points) where an enhancement is observed in the data. This feature becomes more pronounced when dealing with the electric GP and will be further discussed in the next section. It should be noted that all measurements are performed at high ϵ, around 0.9, except the MAMI points which are at $\epsilon \simeq 0.6$. However, this change in ϵ can hardly account for the observed enhancement near $Q^2 \simeq 0.3$ GeV^2, since P_{TT} is expected to be a very small quantity (cf. Fig. 21).

For the second structure function P_{LT}, we note that at our highest Q^2 (1.76 GeV^2) the measured value is almost zero within errors (especially the LEX result). It is suggestive of the limitations of the present extraction methods, with respect to higher-momentum transfers. Turning back to the low-Q^2 region, most models predict an extremum of P_{LT}. This feature is more or less confirmed by experiment, but error bars are still large and can hopefully be reduced in the future. The global behavior of P_{LT} essentially reflects the Q^2 dependence of the magnetic GP β_M, which will be discussed in the next section.

There are no measurements of the spin part of the structure functions, P_{TT} and P_{LTspin}. Theoretical estimates are given in Fig. 21. In HBChPT the spin GPs have been calculated up to order $O(p^4)$ [62,63], i.e., one more order than for the scalar GPs, but the calculation does not show good convergence (cf. curves 2a and 2b in Fig. 21). This should be kept in mind when considering Fig. 20: The good agreement between the low-Q^2 data and HBChPT at $O(p^3)$ may be accidental and not so well verified at next order. In Fig. 21 the DR calculation gives (parameter-free) spin structure functions of very small magnitude, decreasing rapidly with Q^2 and almost independent of the set of πN multipoles. This contribution is also drawn in Fig. 20 as the dotted lines. It amounts to 35–50% of the measured structure functions in the Q^2 region of our experiment, but this percentage is much smaller at lower Q^2. Experimental information on the spin GPs would be very valuable, but very little is available, due to the difficulty of such experiments [64–66].

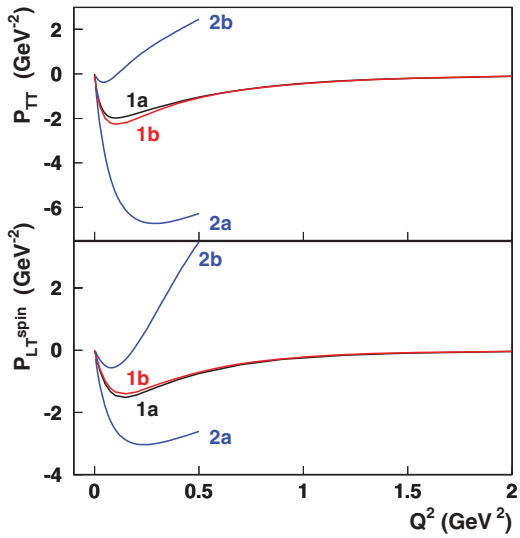

FIG. 21. (Color online) Theoretical predictions for the spin part of the measured structure functions. The DR curves labeled 1a and 1b are calculated with the MAID 2000 and MAID 2003 multipoles, respectively. The HBChPT curves 2a and 2b are obtained at $O(p^3)$ [27] and $O(p^4)$ [62], respectively. They are drawn up to an arbitrary value of $Q^2_{\mathrm{max}} = 0.5$ GeV^2.

C. The electric and magnetic GPs

The data of this experiment allow the extraction of the electric and magnetic GPs of the proton at $Q^2 = 0.92$ and 1.76 GeV^2, as an ultimate step of our analyses. In the DR

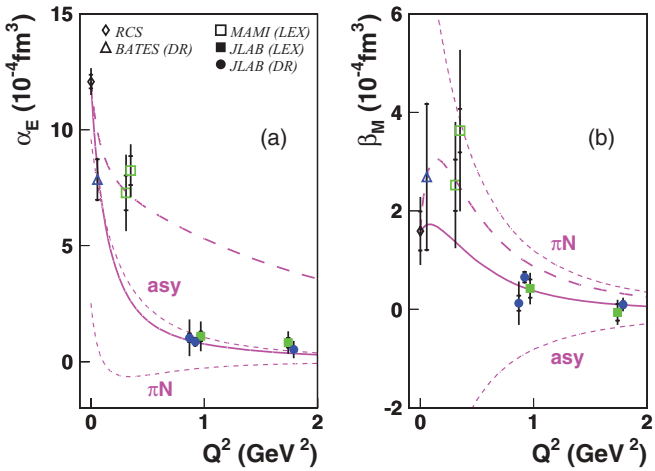

FIG. 22. (Color online) The world data on the electric GP (a) and the magnetic GP (b), with statistical (inner) and total (outer) error bar. The solid curve is the DR calculation drawn for typical parameter values obtained in our experiment: $\Lambda_\alpha = 0.70$ GeV (left) and $\Lambda_\beta = 0.70$ GeV (right). The short-dashed curves show the two separate contributions to this calculation: the pion-nucleon intermediate states (curve labeled "πN") and the [asymptotic + beyond πN] contribution (curve labeled "asy"). The long-dashed curve is the full DR calculation for other parameter values: $\Lambda_\alpha = 1.79$ GeV (left) and $\Lambda_\beta = 0.51$ GeV (right).

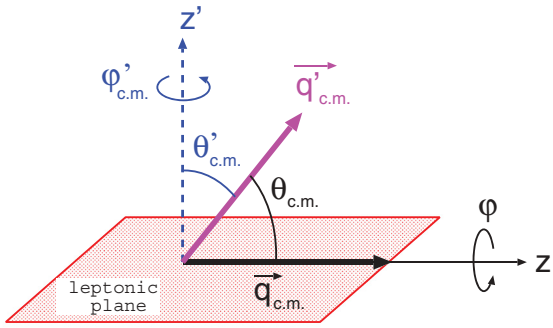

FIG. 23. (Color online) The angular systems to measure the polar and azimuthal angles of the momentum vector $\vec{q}\,'_{\text{c.m.}}$ in the (γp) center of mass.

formalism, these GPs are calculated in a straightforward way, once the $(\Lambda_\alpha, \Lambda_\beta)$ parameters are known ("direct DR extraction"). On the other hand, in the LEX formalism there is no such direct determination of the GPs. The spin structure functions P_{TT} and P_{LTspin} have first to be subtracted from the measured ones, $P_{LL} - P_{TT}/\epsilon$ and P_{LT}, using a model. For this task it is most natural to choose the DR model, especially in our Q^2 range. Once this subtraction is done, the last step is to remove the Q^2 dependence due to the electric form factor G_E^p in the scalar part [cf. Eq. (4)]. Our results for $\alpha_E(Q^2)$ and $\beta_M(Q^2)$, following this procedure, are reported in Table IX, together with the results of the direct DR extraction.

Figure 22 summarizes the existing measurements of $\alpha_E(Q^2)$ and $\beta_M(Q^2)$ of the proton. It is clear that this picture is to some extent (DR)model dependent; for consistency, theoretical curves are drawn only for this particular model. Similarly to Fig. 20, a single DR curve cannot reproduce all the experimental data, and an enhancement can be seen in the region of the MAMI points. In a recent paper interpreting the GPs in the light-front formalism [22], the electric GP is described by adding to the DR calculation a Gaussian contribution centered near $Q^2 = 0.3\ \text{GeV}^2$. With this parametrization, one is able to reproduce the measured $P_{LL} - P_{TT}/\epsilon$ over the full Q^2 range, and the induced electric polarization in the nucleon is shown to extend to larger transverse distances. However, in Ref. [22], no clear physical origin is associated to this additional and intriguing structure in $\alpha_E(Q^2)$.

In the DR model, each scalar GP is the sum of two terms (cf. Sec. II D): the dispersion integrals, saturated by the πN contribution, and the [asymptotic + beyond πN] contribution $\Delta\alpha$ or $\Delta\beta$. Figure 22 shows these two contributions

TABLE X. The phase-space variables (first column), the bin size and the points P_0 at which the cross section is determined (second column). These points are chosen at the middle of the bin, except for the last bin in $q'_{\text{c.m.}}$ and the first bin in $\theta'_{\text{c.m.}}$.

Data sets I-a and II	
ϵ	Fixed at 0.950 (0.879) for data set I-a (II)
$q_{\text{c.m.}}$	Fixed at 1.080 (1.625) GeV/c for data set I-a (II)
$q'_{\text{c.m.}}$	6 bins: regular from 30 to 180, + [180, 250] MeV/c
	6 points: 45, 75, 105, 135, 165, 215 MeV/c
$\theta'_{\text{c.m.}}$	2 bins: $[0°, 60°] \cup [120°, 180°]$; $[60°, 90°] \cup [90°, 120°]$
	2 points: 40° (+ out-of-plane) and 90° (+ in-plane)
$\varphi'_{\text{c.m.}}$	20 bins: regular from −180° to +180°
	20 points: −171°, −153°, −135°, . . . , +153°, +171°
Data set I-b (cf. ref. [6])	
k_{lab}	Fixed at 4.032 GeV
Q^2	Fixed at 1.0 GeV^2
W	15 bins: regular from 0.98 GeV to 1.28 GeV
	15 points: 0.99, 1.01, 103, . . . , 1.25, 1.27 GeV
$\cos\theta_{\text{c.m.}}$	3 bins: [−1, −0.95], [−0.95, −0.80], [−0.80, −0.50]
	3 points: −0.975, −0.875, −0.650
φ	6 bins: regular from 0 to 180°
	6 points: 15°, 45°, 75°, 105°, 135°, 165°

TABLE XI. Detailed systematic errors on the structure functions in the LEX analysis. To obtain the total systematic error, the three partial contributions are first symmetrized (+/−) and then added in quadrature.

Source of systematic error	$\Delta(P_{LL} - P_{TT}/\epsilon)$ (GeV^{-2})	$\Delta(P_{LT})$ (GeV^{-2})
	Data set I-a	
Normalization (±3 %)	+0.505 −0.505	+0.046 −0.046
Beam energy (±2 MeV)	+0.391 −0.354	+0.132 −0.024
Spec. angle (±0.5 mr)	+0.301 −0.301	+0.148 −0.148
Total syst. error	±0.696	±0.174
	Data set II	
Normalization (±3%)	+0.142 −0.142	+0.004 −0.004
Beam energy (±2 MeV)	+0.139 −0.074	+0.017 −0.005
Spec. angle (±0.5 mr)	+0.096 −0.096	+0.054 −0.054
Total syst. error	±0.202	±0.055

TABLE XII. Detailed systematic errors on the parameters Λ_α and Λ_β in the DR analysis. To obtain the total systematic error, the three partial contributions are first symmetrized (+/−) and then added in quadrature.

Source of system error	$\Delta(\Lambda_\alpha)$ (GeV)	$\Delta(\Lambda_\beta)$ (GeV)
	Data set I-a	
Normalization (±3 %)	+0.105−0.099	+0.068−0.053
Beam energy (±2 MeV)	+0.179−0.067	+0.068−0.018
Spec. angle (±0.5 mr)	+0.072−0.072	+0.087−0.087
Total syst. error	±0.175	±0.114
	Data set II	
Normalization (±3 %)	+0.096−0.127	+0.057−0.056
Beam energy (± 2 MeV)	+0.118−0.047	+0.044−0.017
Spec. angle (± 0.5 mr)	+0.052−0.052	+0.041−0.041
Total syst. error	± ±0.149	±0.077
	Data set I-b	
Normalization (± 3 %)	+0.031−0.041	+0.018−0.014
Beam energy (± 2 MeV)	+0.017−0.003	+0.011−0.012
Spec. angle (± 0.5 mr)	+0.005−0.005	+0.012−0.012
Total syst. error	± ±0.037	±0.023

TABLE XIII. The measured ($ep \to ep\gamma$) cross section $d^5\sigma/dk'_{\rm elab}d\Omega'_{\rm elab}d\Omega_{\gamma\rm c.m.}$, in pb/(GeV sr^2), for data set I-a below the pion threshold. The out-of-plane (respectively, in-plane) data correspond to $\theta'_{\rm c.m.} = 40^\circ$ (respectively, 90°). The error $\Delta\sigma$ is statistical only. The ($ep \to ep\gamma$) kinematics are entirely determined by the five variables ($q_{\rm c.m.}$, ϵ, $q'_{\rm c.m.}$, $\theta'_{\rm c.m.}$, $\varphi'_{\rm c.m.}$).

At fixed $q_{\rm c.m.} = 1.080$ GeV/c, fixed $\epsilon = 0.950$, and fixed $Q^2 = 0.92$ GeV^2						
$\theta_{\rm c.m.}$ (°)	φ (°)	$\theta'_{\rm c.m.}$ (°)	$\varphi'_{\rm c.m.}$ (°)	$d^5\sigma \pm \Delta\sigma_{\rm stat}$ at $q'_{\rm c.m.} = 45$ MeV/c	$d^5\sigma \pm \Delta\sigma_{\rm stat}$ at $q'_{\rm c.m.} = 75$ MeV/c	$d^5\sigma \pm \Delta\sigma_{\rm stat}$ at $q'_{\rm c.m.} = 105$ MeV/c
50.6	82.5	40	9	105.5 ± 12.0	68.0 ± 5.0	48.7 ± 3.9
55.1	69.1	40	27	102.6 ± 17.2	75.5 ± 6.1	53.9 ± 4.5
63.0	59.3	40	45	141.8 ± 31.0	114.5 ± 10.2	75.0 ± 6.2
73.0	53.2	40	63	130.5 ± 51.3	123.9 ± 16.3	117.1 ± 11.4
84.2	50.3	40	81	263.7 ± 116.3	238.1 ± 33.9	187.2 ± 19.3
95.8	50.3	40	99	536.3 ± 233.1	417.2 ± 62.5	243.8 ± 28.2
107.0	53.2	40	117	1210.1 ± 425.1	445.1 ± 67.2	300.8 ± 32.1
117.0	59.3	40	135	1389.4 ± 306.0	491.4 ± 59.2	291.8 ± 25.2
124.9	69.1	40	153	619.3 ± 127.0	458.1 ± 39.1	247.0 ± 15.8
129.4	82.5	40	171	570.7 ± 80.2	340.9 ± 21.7	219.7 ± 10.5
129.4	97.5	40	−171	556.9 ± 50.4	318.1 ± 13.9	204.4 ± 8.4
124.9	110.9	40	−153	576.2 ± 34.1	286.3 ± 10.3	191.9 ± 9.2
117.0	120.7	40	−135	443.0 ± 21.2	248.7 ± 8.9	149.2 ± 8.6
107.0	126.8	40	−117	367.7 ± 15.9	196.3 ± 8.0	130.4 ± 8.1
95.8	129.7	40	−99	281.8 ± 12.7	155.0 ± 7.1	93.2 ± 6.1
84.2	129.7	40	−81	242.8 ± 11.7	119.6 ± 6.0	88.7 ± 5.4
73.0	126.8	40	−63	166.5 ± 9.6	106.4 ± 5.5	57.1 ± 3.9
63.0	120.7	40	−45	120.2 ± 8.3	73.8 ± 4.3	50.7 ± 3.6
55.1	110.9	40	−27	108.3 ± 8.6	60.9 ± 4.2	48.5 ± 3.5
50.6	97.5	40	−9	107.7 ± 9.5	55.8 ± 4.0	36.5 ± 3.1
9.0	0.0	90	9	9.5 ± 2.4	15.6 ± 2.3	23.1 ± 3.3
27.0	0.0	90	27	7.2 ± 3.0	12.8 ± 2.2	12.6 ± 2.3
153.0	0.0	90	153	33.6 ± 8.6	11.9 ± 3.5	8.8 ± 2.7
171.0	0.0	90	171	11.3 ± 2.5	10.6 ± 1.4	9.8 ± 1.0
171.0	180.0	90	−171	258.4 ± 25.8	128.6 ± 7.6	89.6 ± 5.1
153.0	180.0	90	−153	553.1 ± 30.7	286.1 ± 10.5	178.7 ± 10.0
135.0	180.0	90	−135	468.1 ± 18.8	266.0 ± 10.1	167.6 ± 11.7
117.0	180.0	90	−117	402.3 ± 14.1	231.1 ± 9.8	149.4 ± 10.3
99.0	180.0	90	−99	286.8 ± 11.2	159.0 ± 8.1	99.3 ± 6.3
81.0	180.0	90	−81	194.5 ± 9.0	95.6 ± 5.4	62.6 ± 4.0
63.0	180.0	90	−63	121.8 ± 7.2	62.4 ± 4.1	50.8 ± 3.6
45.0	180.0	90	−45	74.1 ± 5.7	46.6 ± 3.3	30.2 ± 2.8
27.0	180.0	90	−27	39.7 ± 4.1	31.4 ± 2.6	23.2 ± 2.8
9.0	180.0	90	−9	17.7 ± 2.7	27.5 ± 2.8	18.6 ± 2.7

separately (short-dashed curves). For the electric GP the [asymptotic + beyond πN] term is by far dominant at every Q^2. For the magnetic GP the two contributions are large and of opposite sign. The πN dispersive integral is of paramagnetic nature, namely via the formation of the $\Delta(1232)$ resonance. The diamagnetism ("asy" curve) arises from the $\Delta\beta$ term associated with the exchange of the σ meson ($=[\pi\pi]_0$) in the t channel. The two terms strongly cancel, leading to an overall small polarizability and a more or less pronounced extremum in the low-Q^2 region.

It is well known that nucleon polarizabilities are closely linked to the mesonic cloud, an essential ingredient of nucleon structure since the first ChPT calculation of α_E and β_M in RCS [67]. The mesonic cloud is also expected to play an important role in the GPs. The measured value of the mean-square electric polarizability radius of the proton $\langle r^2_\alpha \rangle$, of about 2 fm^2 [8], clearly indicates that what is probed in VCS is a large-size structure. The nontrivial shape observed for the electric GP over the full Q^2 range calls for further understanding, and more measurements of the scalar GPs in the Q^2 region of [0–1] GeV^2 are needed to get a clearer picture. Such measurements are underway at MAMI [68].

VI. CONCLUSION

The JLab E93-050 experiment was one of the first-generation VCS experiments, dedicated in part to the measurement of the generalized polarizabilities of the proton at high-momentum transfer. It was a challenging task to exploit the Hall A equipment in its commissioning phase to study

TABLE XIV. Same as in previous table but for data set II below the pion threshold.

At fixed $q_{\text{c.m.}} = 1.625$ GeV/c, fixed $\epsilon = 0.879$, and fixed $Q^2 = 1.76$ GeV^2						
$\theta_{\text{c.m.}}$ (°)	φ (°)	$\theta'_{\text{c.m.}}$ (°)	$\varphi'_{\text{c.m.}}$ (°)	$d^5\sigma \pm \Delta\sigma_{\text{stat}}$ at $q'_{\text{c.m.}} = 45$ MeV/c	$d^5\sigma \pm \Delta\sigma_{\text{stat}}$ at $q'_{\text{c.m.}} = 75$ MeV/c	$d^5\sigma \pm \Delta\sigma_{\text{stat}}$ at $q'_{\text{c.m.}} = 105$ MeV/c
50.6	82.5	40	9	9.3 ± 1.2	5.6 ± 0.6	2.9 ± 0.4
55.1	69.1	40	27	8.0 ± 1.5	5.0 ± 0.7	3.7 ± 0.6
63.0	59.3	40	45	6.9 ± 2.0	7.1 ± 1.2	5.4 ± 0.9
73.0	53.2	40	63	16.5 ± 4.8	8.8 ± 1.7	7.6 ± 1.6
84.2	50.3	40	81	10.3 ± 5.6	15.7 ± 3.3	9.1 ± 1.9
95.8	50.3	40	99	80.2 ± 21.1	30.5 ± 5.4	25.5 ± 4.1
107.0	53.2	40	117	87.2 ± 23.2	40.1 ± 6.8	26.1 ± 4.1
117.0	59.3	40	135	122.5 ± 25.9	42.5 ± 6.0	31.1 ± 3.8
124.9	69.1	40	153	140.5 ± 25.3	51.1 ± 6.1	27.0 ± 2.8
129.4	82.5	40	171	62.2 ± 12.0	38.9 ± 3.7	25.1 ± 2.3
129.4	97.5	40	−171	74.3 ± 9.2	34.3 ± 2.3	20.1 ± 1.5
124.9	110.9	40	−153	51.7 ± 4.6	33.1 ± 1.6	18.6 ± 0.9
117.0	120.7	40	−135	42.4 ± 2.9	25.4 ± 1.2	15.3 ± 0.8
107.0	126.8	40	−117	36.1 ± 2.2	18.9 ± 0.9	10.6 ± 0.7
95.8	129.7	40	−99	28.4 ± 1.7	12.8 ± 0.7	7.0 ± 0.6
84.2	129.7	40	−81	19.4 ± 1.6	10.1 ± 0.7	6.5 ± 0.6
73.0	126.8	40	−63	14.5 ± 1.5	7.2 ± 0.6	3.7 ± 0.4
63.0	120.7	40	−45	10.6 ± 1.2	5.5 ± 0.5	3.9 ± 0.5
55.1	110.9	40	−27	8.4 ± 1.1	6.3 ± 0.6	3.2 ± 0.5
50.6	97.5	40	−9	9.0 ± 1.3	3.9 ± 0.5	3.6 ± 0.5
9.0	0.0	90	9	1.5 ± 0.5	1.3 ± 0.4	1.1 ± 0.3
27.0	0.0	90	27	1.2 ± 0.7	0.7 ± 0.3	1.3 ± 0.4
171.0	0.0	90	171	5.3 ± 1.2	1.6 ± 0.4	0.9 ± 0.2
171.0	180.0	90	−171	39.9 ± 7.3	25.5 ± 2.4	15.8 ± 1.1
153.0	180.0	90	−153	64.1 ± 6.0	44.7 ± 2.1	26.4 ± 1.1
135.0	180.0	90	−135	65.6 ± 3.7	32.2 ± 1.3	19.9 ± 0.9
117.0	180.0	90	−117	42.6 ± 2.1	20.8 ± 0.9	12.7 ± 0.8
99.0	180.0	90	−99	24.4 ± 1.3	12.8 ± 0.7	8.3 ± 0.7
81.0	180.0	90	−81	14.1 ± 0.9	8.2 ± 0.6	4.5 ± 0.5
63.0	180.0	90	−63	10.7 ± 0.8	5.5 ± 0.5	3.5 ± 0.5
45.0	180.0	90	−45	7.4 ± 0.8	3.8 ± 0.4	2.1 ± 0.4
27.0	180.0	90	−27	3.4 ± 0.6	3.2 ± 0.4	2.1 ± 0.4
9.0	180.0	90	−9	2.8 ± 0.7	1.8 ± 0.4	0.9 ± 0.3

the exclusive process $ep \to ep\gamma$ and accurately measure its small cross section. Two methods have been used to extract the physics observables: one model-independent based on the LEX and one model-dependent based on the DR formalism. The results of the two methods show good consistency at the level of the VCS structure functions $P_{LL} - P_{TT}/\epsilon$ and P_{LT}.

The data obtained in this experiment allow in a unique way to put in perspective the regions of high- and low-momentum transfer. The results are an essential piece to build a more complete picture of the electric and magnetic GPs of the proton as a function of Q^2, i.e., ultimately the nucleon's polarization response as a function of the distance scale. The electric GP does not seem to have a smooth falloff, and the behavior of the magnetic GP quantifies the detailed contributions of para- and diamagnetism in the proton. Experimental data are still scarce, and more measurements are desirable in order to improve our understanding of these fundamental observables. This is especially true at low Q^2, where the prominent role of the mesonic cloud can be probed. New VCS experiments, together with new RCS experiments and theoretical developments in the field, should provide a step forward in our understanding of the electromagnetic structure of the nucleon.

ACKNOWLEDGMENTS

We thank the JLab accelerator staff and the Hall A technical staff for their dedication in performing this experiment and making it a success. This work was supported by DOE Contract No. DE-AC05-84ER40150 under which the Southeastern Universities Research Association (SURA) operates the Thomas Jefferson National Accelerator Facility. We acknowledge additional grants from the US DOE and NSF, the French CNRS and CEA, the Conseil Régional d'Auvergne, the FWO-Flanders (Belgium), and the BOF-Ghent University.

TABLE XV. Same as in previous table but for data set I-a above the pion threshold.

At fixed $q_{\text{c.m.}} = 1.080$ GeV/c, fixed $\epsilon = 0.950$, and fixed $Q^2 = 0.92$ GeV^2						
$\theta_{\text{c.m.}}$ (°)	φ (°)	$\theta'_{\text{c.m.}}$ (°)	$\varphi'_{\text{c.m.}}$ (°)	$d^5\sigma \pm \Delta\sigma_{\text{stat}}$ at $q'_{\text{c.m.}} = 135$ MeV/c	$d^5\sigma \pm \Delta\sigma_{\text{stat}}$ at $q'_{\text{c.m.}} = 165$ MeV/c	$d^5\sigma \pm \Delta\sigma_{\text{stat}}$ at $q'_{\text{c.m.}} = 215$ MeV/c
50.6	82.5	40	9	38.8 ± 5.2	32.8 ± 20.6	
55.1	69.1	40	27	44.5 ± 5.9	53.6 ± 18.1	
63.0	59.3	40	45	54.2 ± 6.1	43.8 ± 10.1	
73.0	53.2	40	63	91.4 ± 11.6	97.5 ± 21.9	
84.2	50.3	40	81	91.1 ± 15.5	168.3 ± 42.7	
95.8	50.3	40	99	175.5 ± 26.2	143.0 ± 38.8	159.6 ± 95.1
107.0	53.2	40	117	229.0 ± 28.7	169.4 ± 33.4	168.8 ± 72.4
117.0	59.3	40	135	193.8 ± 19.9	153.2 ± 19.6	157.1 ± 24.9
124.9	69.1	40	153	184.4 ± 14.0	124.1 ± 11.3	119.7 ± 14.6
129.4	82.5	40	171	178.5 ± 12.1	125.2 ± 12.6	125.5 ± 18.3
129.4	97.5	40	–171	121.4 ± 9.9	127.1 ± 14.3	155.6 ± 39.6
124.9	110.9	40	−153	153.8 ± 13.4	81.2 ± 19.4	
117.0	120.7	40	−135	90.2 ± 11.3	141.0 ± 29.3	
107.0	126.8	40	−117	74.7 ± 8.6	80.7 ± 28.3	
95.8	129.7	40	−99	67.3 ± 7.0	71.9 ± 33.1	
84.2	129.7	40	−81	69.9 ± 8.2	36.0 ± 33.9	
73.0	126.8	40	−63	32.2 ± 4.7		
63.0	120.7	40	−45	45.5 ± 6.0		
55.1	110.9	40	−27	33.9 ± 5.3		
50.6	97.5	40	−9	41.2 ± 5.9		
9.0	0.0	90	9	14.9 ± 5.6		
27.0	0.0	90	27	22.7 ± 6.2		
45.0	0.0	90	45	18.1 ± 8.2		
135.0	0.0	90	135			176.9 ± 75.4
153.0	0.0	90	153	7.2 ± 1.7	16.5 ± 3.0	80.1 ± 12.6
171.0	0.0	90	171	14.6 ± 1.8	31.1 ± 4.5	79.7 ± 17.9
171.0	180.0	90	−171	84.5 ± 7.8	94.0 ± 11.8	216.1 ± 70.3
153.0	180.0	90	−153	137.6 ± 12.8	176.5 ± 52.7	
135.0	180.0	90	−135	112.2 ± 16.3		
117.0	180.0	90	−117	61.8 ± 9.8		
99.0	180.0	90	−99	56.3 ± 14.4		
81.0	180.0	90	−81	45.8 ± 20.3		
27.0	180.0	90	−27	28.1 ± 10.4		
9.0	180.0	90	−9	30.8 ± 9.3		

We thank the INT (Seattle) and ECT* (Trento) for the organization of VCS workshops.

APPENDIX A: KINEMATICS AND BINNING

The GPs depend on $q_{\text{c.m.}}$, or equivalently on the four-momentum transfer squared Q^2 taken in the limit $q'_{\text{c.m.}} \to 0$ [9]. This variable is defined as $\tilde{Q}^2 = 2m_p(\sqrt{m_p^2 + {q_{\text{c.m.}}}^2} - m_p)$. It has been denoted Q^2 throughout the paper for simplicity.

Two angular systems in the CM are described in Sec. IV G: "standard" and "rotated." In the standard system, the polar angle $\theta_{\text{c.m.}}$ is measured with respect to the z axis aligned with the $\vec{q}_{\text{c.m.}}$ vector. In the rotated system, the polar angle $\theta'_{\text{c.m.}}$ is measured with respect to the z' axis orthogonal to the leptonic plane; see Fig. 23. In-plane kinematics correspond to $\theta'_{\text{c.m.}} = 90°$ or to $\varphi = 0°$ and 180°. The conversion formulas between the two systems are as follows:

$$\begin{aligned} \cos\theta'_{\text{c.m.}} &= \sin\theta_{\text{c.m.}} \sin\varphi, \\ \cos\varphi'_{\text{c.m.}} &= \cos\theta_{\text{c.m.}} / \sin\theta'_{\text{c.m.}}, \\ \sin\varphi'_{\text{c.m.}} &= \sin\theta_{\text{c.m.}} \cos\varphi / \sin\theta'_{\text{c.m.}}. \end{aligned} \tag{A1}$$

Table X gives the binning information for the three data sets. The variables which are kept fixed differ for (I-a and II) and for (I-b). The three first bins in $q'_{\text{c.m.}}$ are below the pion threshold, and the other ones are above. For $\theta'_{\text{c.m.}}$, the up-down symmetry with respect to the leptonic plane allows to sum the intervals as indicated (∪ symbol). This up+down sum is also applied in the φ bins of data set I-b.

TABLE XVI. Same as in previous table but for data set II above the pion threshold.

at fixed $q_{\text{c.m.}} = 1.625$ GeV/c, fixed $\epsilon = 0.879$, and fixed $Q^2 = 1.76$ GeV^2						
$\theta_{\text{c.m.}}$ (°)	φ (°)	$\theta'_{\text{c.m.}}$ (°)	$\varphi'_{\text{c.m.}}$ (°)	$d^5\sigma \pm \Delta\sigma_{\text{stat}}$ at $q'_{\text{c.m.}} = 135$ MeV/c	$d^5\sigma \pm \Delta\sigma_{\text{stat}}$ at $q'_{\text{c.m.}} = 165$ MeV/c	$d^5\sigma \pm \Delta\sigma_{\text{stat}}$ at $q'_{\text{c.m.}} = 215$ MeV/c
50.6	82.5	40	9	2.3 ± 0.5		
55.1	69.1	40	27	3.8 ± 0.7	2.8 ± 1.1	
63.0	59.3	40	45	4.1 ± 0.8	3.4 ± 1.1	
73.0	53.2	40	63	5.0 ± 1.4	5.3 ± 2.0	
84.2	50.3	40	81	7.9 ± 2.1	4.2 ± 2.4	
95.8	50.3	40	99	10.8 ± 2.6	19.7 ± 5.9	9.3 ± 5.1
107.0	53.2	40	117	18.3 ± 2.8	9.1 ± 2.1	14.4 ± 3.4
117.0	59.3	40	135	21.3 ± 2.7	13.9 ± 2.3	9.9 ± 2.1
124.9	69.1	40	153	18.0 ± 2.0	15.0 ± 1.8	12.3 ± 1.6
129.4	82.5	40	171	17.1 ± 1.3	13.6 ± 1.1	8.8 ± 0.8
129.4	97.5	40	−171	18.2 ± 1.0	13.2 ± 0.9	8.6 ± 0.7
124.9	110.9	40	−153	14.3 ± 0.8	9.7 ± 0.8	8.0 ± 1.2
117.0	120.7	40	−135	9.7 ± 0.7	9.5 ± 1.1	8.7 ± 2.6
107.0	126.8	40	−117	7.5 ± 0.7	5.0 ± 1.0	
95.8	129.7	40	−99	6.2 ± 0.7	8.0 ± 2.2	
84.2	129.7	40	−81	5.6 ± 0.8	2.6 ± 1.2	
73.0	126.8	40	−63	4.0 ± 0.7	4.9 ± 2.9	
63.0	120.7	40	−45	3.3 ± 0.7	5.2 ± 3.0	
55.1	110.9	40	−27	2.0 ± 0.5	2.3 ± 1.5	
50.6	97.5	40	−9	3.9 ± 0.9		
9.0	0.0	90	9	1.9 ± 1.0		
27.0	0.0	90	27	0.7 ± 0.4		
153.0	0.0	90	153			3.7 ± 1.3
171.0	0.0	90	171	1.4 ± 0.2	1.7 ± 0.2	4.2 ± 0.4
171.0	180.0	90	−171	12.7 ± 0.8	10.1 ± 0.7	9.5 ± 0.7
153.0	180.0	90	−153	19.1 ± 0.9	14.4 ± 1.0	13.6 ± 1.9
135.0	180.0	90	−135	13.1 ± 0.8	10.3 ± 1.5	
117.0	180.0	90	−117	8.6 ± 0.9		
99.0	180.0	90	−99	6.2 ± 1.1		
81.0	180.0	90	−81	1.3 ± 0.7		
63.0	180.0	90	−63	4.3 ± 2.6		
9.0	180.0	90	−9	3.5 ± 1.7		

APPENDIX B: SYSTEMATIC ERRORS

This Appendix gives details on the systematic errors on the primary observables extracted from the cross-section data: the structure functions in the LEX analysis (Table XI) and the $(\Lambda_\alpha, \Lambda_\beta)$ parameters in the DR analysis (Table XII). The systematic errors on all other extracted observables are derived from these ones by error propagation. The origin of the 3% normalization error in these tables is explained in Sec. IV I.

APPENDIX C: CROSS SECTION TABLES

This appendix gives our measured values of the photon electroproduction cross section. Table XIII (respectively, Table XIV) is for data set I-a (respectively, II) below the pion threshold. Table XV (respectively, Table XVI) is for data set I-a (respectively, II) above the pion threshold. In these four tables, the errors are statistical only (in rms); the systematic error is discussed in the text (Sec. IV H).

The cross-section values for data set I-b can be found partly in Ref. [6], but there some settings of data set I-a were also included. Thus, for the sake of completeness, the cross-section values corresponding to the DR analysis (I-b) of the present paper are reported here in Table XVII. It should be noted that this cross section has been determined at $Q^2 = 1.0$ GeV^2 (instead of 0.92 GeV^2), as part of a wider study program at $Q^2 = 1$ GeV^2 [6]. To obtain the VCS observables at $Q^2 = 0.92$ GeV^2 from the "I-b" DR fit, we have explicitly assumed that the $(\Lambda_\alpha, \Lambda_\beta)$ parameters have no significant variation *locally* in Q^2. Then we simply use the parameter values of Table VI (I-b part), fitted at $Q^2 = 1.0$ GeV^2, as inputs to the DR calculation of the VCS observables at $Q^2 = 0.92$ GeV^2.

Ascii files of Tables XIII to XVII will be added as auxiliary files to this paper, see Ref. [69]. They are also available at URLs: http://userweb.jlab.org/~helene/paper_vcs_gps_2012/all-ascii-tables and http://clrwww.in2p3.fr/sondem/E93050-tables-GPS or on request to the authors.

TABLE XVII. The measured ($ep \to ep\gamma$) cross section $d^5\sigma/dk'_{\rm elab}d\Omega'_{\rm elab}d\Omega_{\gamma\rm c.m.}$ ($\pm$statistical error $\pm$systematic error) in pb/(GeV sr^2), for data set I-b. The ($ep \to ep\gamma$) kinematics are entirely determined by the five variables: Q^2 (= 1.0 GeV^2 fixed), beam energy $E_{\rm beam}$ (= 4.032 GeV fixed), and (W, $\cos\theta_{\rm c.m.}$, φ) which are given in the table. Numbers in parenthesis represent a rough estimate of the systematic error, when missing.

W (GeV)	$\varphi = 15^\circ$	$\varphi = 45^\circ$	$\varphi = 75^\circ$	$\varphi = 105^\circ$	$\varphi = 135^\circ$	$\varphi = 165^\circ$
			$\cos\theta_{\rm c.m.} = -0.975$			
1.05						140 ± 73 ± 62
1.07				69 ± 41 ± 18	63 ± 24 ± 25	120 ± 30 ± 24
1.09			50 ± 32 ± 9	91 ± 24 ± 10	92 ± 20 ± 12	86 ± 19 ± 24
1.11		94 ± 40 ± 2	53 ± 17 ± 9	114 ± 20 ± 11	110 ± 21 ± 9	61 ± 16 ± 18
1.13		36 ± 14 ± 7	54 ± 14 ± 15	75 ± 16 ± 8	72 ± 17 ± 17	53 ± 16 ± 3
1.15	43 ± 14 ± 15	95 ± 18 ± 15	96 ± 17 ± 9	97 ± 18 ± 14	131 ± 23 ± 43	104 ± 19 ± 27
1.17	55 ± 13 ± 9	112 ± 18 ± 8	102 ± 17 ± 12	124 ± 18 ± 9	179 ± 22 ± 24	168 ± 22 ± 10
1.19	93 ± 16 ± 7	116 ± 17 ± 13	136 ± 18 ± 13	154 ± 18 ± 23	145 ± 19 ± 14	178 ± 24 ± 15
1.21	118 ± 18 ± 17	116 ± 17 ± 20	167 ± 18 ± 9	119 ± 15 ± 10	152 ± 21 ± 6	144 ± 24 ± 20
1.23	111 ± 16 ± 13	109 ± 15 ± 18	102 ± 13 ± 11	141 ± 16 ± 8	107 ± 17 ± 18	83 ± 15 ± 14
1.25	51 ± 11 ± 12	78 ± 12 ± 11	94 ± 12 ± 11	74 ± 13 ± 10	81 ± 11 ± 6	96 ± 12 ± 10
1.27	41 ± 9 ± 7	51 ± 9 ± 6	48 ± 9 ± 6	64 ± 9 ± 4	61 ± 8 ± 4	47 ± 7 ± 5
			$\cos\theta_{\rm c.m.} = -0.875$			
1.05					296 ± 90 ± 18	103 ± 37 ± 11
1.07				169 ± 53 ± 12	163 ± 36 ± 6	139 ± 30 ± 14
1.09			374 ± 163 ± 9	98 ± 25 ± 40	113 ± 25 ± 14	122 ± 29 ± 11
1.11			107 ± 32 ± 8	129 ± 24 ± 10	119 ± 28 ± 13	58 ± 23 ± 45
1.13			91 ± 21 ± 6	123 ± 24 ± 4	68 ± 21 ± 16	99 ± 31 ± 11
1.15		81 ± 29 ± 12	143 ± 23 ± 9	97 ± 20 ± 18	99 ± 22 ± 13	117 ± 25 ± 10
1.17		38 ± 15 ± 15	99 ± 18 ± 5	106 ± 18 ± 11	118 ± 22 ± 14	106 ± 30 ± 14
1.19	172 ± 44 ± 26	112 ± 19 ± 8	127 ± 18 ± 11	125 ± 18 ± 12	145 ± 29 ± 18	272 ± 122 ± 90
1.21	103 ± 22 ± 11	123 ± 19 ± 7	134 ± 17 ± 5	183 ± 21 ± 11	178 ± 51 ± 18	217 ± 70 ± 46
1.23	129 ± 21 ± 8	117 ± 18 ± 6	135 ± 16 ± 9	133 ± 20 ± 12	130 ± 24 ± 42	68 ± 19 ± 28
1.25	99 ± 17 ± 6	95 ± 17 ± 6	99 ± 13 ± 7	68 ± 14 ± 8	88 ± 14 ± 14	81 ± 21 ± 8
1.27	54 ± 13 ± 7	60 ± 13 ± 14	87 ± 13 ± 5	71 ± 11 ± 6	57 ± 12 ± 7	
			$\cos\theta_{\rm c.m.} = -0.650$			
1.03						287 ± 103 ± 11
1.05				201 ± 177 ± 16	211 ± 58 ± 14	188 ± 46 ± 9
1.07				191 ± 52 ± 10	112 ± 28 ± 11	131 ± 31 ± 20
1.09				150 ± 31 ± 9	110 ± 26 ± 10	72 ± 32 ± 101
1.11			114 ± 36 ± 5	108 ± 22 ± 7	179 ± 46 ± 41	153 ± 77 ± (120)
1.13			115 ± 25 ± 5	139 ± 27 ± 7	62 ± 24 ± 515	78 ± 32 ± (120)
1.15			86 ± 18 ± 5	116 ± 23 ± 11	128 ± 27 ± 169	91 ± 36 ± (120)
1.17		145 ± 48 ± 13	149 ± 21 ± 10	137 ± 22 ± 15	132 ± 33 ± 400	
1.19		129 ± 30 ± 24	169 ± 21 ± 5	152 ± 22 ± 27	178 ± 69 ± (200)	
1.21		175 ± 28 ± 22	152 ± 19 ± 14	125 ± 21 ± 17		
1.23	66 ± 33 ± (30)	104 ± 19 ± 16	131 ± 17 ± 10	87 ± 21 ± 10	88 ± 38 ± (200)	
1.25	79 ± 23 ± (20)	108 ± 19 ± 12	76 ± 12 ± 12	50 ± 15 ± 59	125 ± 30 ± (200)	
1.27	80 ± 19 ± (20)	107 ± 20 ± 11	102 ± 15 ± 15	85 ± 16 ± 73	89 ± 42 ± (200)	

[1] J. Roche *et al.* (VCS), Phys. Rev. Lett. **85**, 708 (2000).
[2] I. K. Bensafa *et al.* (MAMI-A1), Eur. Phys. J. A **32**, 69 (2007).
[3] P. Janssens *et al.* (MAMI-A1), Eur. Phys. J. A **37**, 1 (2008).
[4] N. F. Sparveris *et al.*, Phys. Rev. C **78**, 018201 (2008).
[5] G. Laveissière *et al.* (Jefferson Lab Hall A), Phys. Rev. Lett. **93**, 122001 (2004).
[6] G. Laveissière *et al.* (Jefferson Lab Hall A), Phys. Rev. C **79**, 015201 (2009).
[7] P. Bourgeois *et al.*, Phys. Rev. Lett. **97**, 212001 (2006).
[8] P. Bourgeois *et al.*, Phys. Rev. C **84**, 035206 (2011).
[9] P. A. M. Guichon and M. Vanderhaeghen, Prog. Part. Nucl. Phys. **41**, 125 (1998).
[10] D. Drechsel, B. Pasquini, and M. Vanderhaeghen, Phys. Rep. **378**, 99 (2003).
[11] B. Pasquini, D. Drechsel, and M. Vanderhaeghen, Eur. Phys. J. **198**, 269 (2011).
[12] N. d'Hose *et al.*, Prog. Part. Nucl. Phys. **44**, 371 (2000).

[13] C. E. Hyde-Wright and K. de Jager, Annu. Rev. Nucl. Part. Sci. **54**, 217 (2004).
[14] H. Fonvieille, Prog. Part. Nucl. Phys. **55**, 198 (2005).
[15] N. d'Hose, Eur. Phys. J. A **28S1**, 117 (2006).
[16] E. Downie and H. Fonvieille, Eur. Phys. J. ST **198**, 287 (2011).
[17] V. Olmos de Leon *et al*., Eur. Phys. J. A **10**, 207 (2001).
[18] R. Berg and C. Lindner, Nucl. Phys. **26**, 259 (1961).
[19] D. Drechsel and H. Arenhövel, Nucl. Phys. A **233**, 153 (1974).
[20] P. A. M. Guichon, G. Q. Liu, and A. W. Thomas, Nucl. Phys. A **591**, 606 (1995).
[21] S. Scherer, AIP Conf. Proc. **768**, 110 (2005).
[22] M. Gorchtein, C. Lorce, B. Pasquini, and M. Vanderhaeghen, Phys. Rev. Lett. **104**, 112001 (2010).
[23] D. Drechsel, G. Knochlein, A. Y. Korchin, A. Metz, and S. Scherer, Phys. Rev. C **57**, 941 (1998).
[24] D. Drechsel, G. Knochlein, A. Y. Korchin, A. Metz, and S. Scherer, Phys. Rev. C **58**, 1751 (1998).
[25] T. R. Hemmert, B. R. Holstein, G. Knochlein, and S. Scherer, Phys. Rev. Lett. **79**, 22 (1997).
[26] T. R. Hemmert, B. R. Holstein, G. Knochlein, and S. Scherer, Phys. Rev. D **55**, 2630 (1997).
[27] T. R. Hemmert, B. R. Holstein, G. Knochlein, and D. Drechsel, Phys. Rev. D **62**, 014013 (2000).
[28] G. Q. Liu, A. W. Thomas, and P. A. M. Guichon, Aust. J. Phys. **49**, 905 (1996).
[29] B. Pasquini, S. Scherer, and D. Drechsel, Phys. Rev. C **63**, 025205 (2001).
[30] B. Pasquini, S. Scherer, and D. Drechsel (2001), arXiv:nucl-th/0105074.
[31] B. Pasquini, D. Drechsel, M. Gorchtein, A. Metz, and M. Vanderhaeghen, Phys. Rev. C **62**, 052201 (2000).
[32] B. Pasquini, M. Gorchtein, D. Drechsel, A. Metz, and M. Vanderhaeghen, Eur. Phys. J. A **11**, 185 (2001).
[33] A. Metz and D. Drechsel, Z. Phys. A **356**, 351 (1996).
[34] A. Metz and D. Drechsel, Z. Phys. A **359**, 165 (1997).
[35] M. Vanderhaeghen, Phys. Lett. B **368**, 13 (1996).
[36] M. Kim and D.-P. Min (1997), arXiv:hep-ph/9704381.
[37] A. I. L'vov, S. Scherer, B. Pasquini, C. Unkmeir, and D. Drechsel, Phys. Rev. C **64**, 015203 (2001).
[38] M. Gorchtein, Phys. Rev. C **81**, 015206 (2010).
[39] D. Djukanovic, Ph.D. thesis, Mainz University, 2008.
[40] M. Vanderhaeghen, Phys. Lett. B **402**, 243 (1997).
[41] D. Drechsel, O. Hanstein, S. S. Kamalov, and L. Tiator, Nucl. Phys. A **645**, 145 (1999).
[42] J. Alcorn *et al*., Nucl. Instrum. Methods A **522**, 294 (2004).
[43] N. Degrande, Ph.D. thesis, Gent University, 2001.
[44] S. Jaminion, Ph.D. thesis, Université Blaise Pascal of Clermont-Fd, 2001.
[45] C. Jutier, Ph.D. thesis, Old Dominion University and Université Blaise Pascal of Clermont-Fd, 2001.
[46] G. Laveissière, Ph.D. thesis, Université Blaise Pascal of Clermont-Fd, 2001.
[47] L. Todor, Ph.D. thesis, Old Dominion University, 2000.
[48] CEBAF Online Data Acquisition (version 1.4), [http://coda.jlab.org].
[49] R. Suleiman (1998), Technical Note, Jlab-TN-98-007.
[50] R. Di Salvo, P. Bertin, and G. Laveissière (2001), Technical Note, Jlab-TN-01-005.
[51] R. Michaels and M. Jones (2000), Report on electronic dead time, [http://www.jlab.org/jones/e91011/report_on_deadtime.ps].
[52] C. Hyde-Wright, L. Todor, and G. Laveissière (2001), Technical Note, Jlab-TN-01-001.
[53] S. Jaminion and H. Fonvieille (2001), Technical Note, Jlab-TN-01-002.
[54] H. Fonvieille (2001), PCCF-RI-0127, [http://hal.in2p3.fr/in2p3-00011090], and PCCF-RI-0128, [http://hal.in2p3.fr/in2p3-00674829].
[55] M. Rvachev (2001), Technical Note, Jlab-TN-01-055.
[56] P. Janssens *et al*., Nucl. Instrum. Methods A **566**, 675 (2006).
[57] M. Vanderhaeghen, J. M. Friedrich, D. Lhuillier, D. Marchand, L. Van Hoorebeke, and J. VandeWiele, Phys. Rev. C **62**, 025501 (2000).
[58] H. Fonvieille (2000), PCCF-RI-0129, [http://hal.in2p3.fr/in2p3-00674846].
[59] E. J. Brash, A. Kozlov, S. Li, and G. M. Huber, Phys. Rev. C **65**, 051001 (2002).
[60] M. K. Jones *et al*. (Jefferson Lab Hall A), Phys. Rev. Lett. **84**, 1398 (2000).
[61] O. Gayou *et al*., Phys. Rev. Lett. **88**, 092301 (2002).
[62] C. W. Kao and M. Vanderhaeghen, Phys. Rev. Lett. **89**, 272002 (2002).
[63] C.-W. Kao, B. Pasquini, and M. Vanderhaeghen, Phys. Rev. D **70**, 114004 (2004).
[64] H. Merkel and N. d'Hose (2000), spokespersons, MAMI Proposal A1/1-00.
[65] P. Janssens, Ph.D. thesis, Gent University, 2007.
[66] L. Doria, Ph.D. thesis, Mainz University, 2007.
[67] V. Bernard, N. Kaiser, A. Schmidt, and U. G. Meissner, Phys. Lett. B **319**, 269 (1993), and references therein.
[68] H. Merkel and H. Fonvieille (2009), spokespersons, MAMI Proposal A1/1-09.
[69] See Supplemental Material at http://link.aps.org/supplemental/10.1103/PhysRevC.86.015210 for Ascii files of Tables XIII to XVII.